Tracking systems for intracranial medical devices: a review

Quentin Francois, Arthur André, Bertrand Duplat, Sinan Haliyo, Stephane Regnier

ORIGINAL ARTICLE

Tracking systems for intracranial medical devices: a review

Quentin François[1,3] | **Arthur André**[2] | **Bertrand Duplat**[3] | **Sinan Haliyo**[1] | **Stéphane Régnier**[1]

[1]Institute of Intelligent and Robotic Systems (ISIR), Sorbonne University, Paris, F-75005, France

[2]Department of Neurosurgery, La Pitié-Salpétrière Hospital, Paris, F-75013, France

[3]Robeauté, Paris, F-75003, France

Correspondence
Quentin François
ISIR, Sorbonne University, Paris, F-75005, France
Robeauté, Paris, F-75003, France
Email: quentin@robeaute.com

Funding information

In minimally-invasive surgery, especially in neurosurgery, the ability to reach deep and functional structures without damage remains a major challenge. Recent breakthroughs in microtechnologies have enabled the downsizing of an increasing number of devices. In such a context, the possibility to navigate a micro-medical device inside the human brain is a reachable ambition. One of the most expected applications is the identification and the treatment of early stage cancers which could strongly improve therapies efficiency. Despite these remarkable attainments, micromachines, to actually become revolutionary, require a tracking system at least as accurate as its size and working in an heterogeneous environment. The aim of the present paper is to provide an overview of the state of the art in medical device tracking systems for the brain. Firstly, the latest advances are categorized by technological family: magnetic field, electromagnetic waves, magnetic resonance, ultrasound waves and hybrid solutions. Secondly, in a comparative purpose, performance criteria are evaluated and displayed in radar diagrams and graphs to highlight the three dimensions challenge the systems should take up: performance, invasiveness and user experience. Finally, the present and future of each localisation family are provided.

KEYWORDS

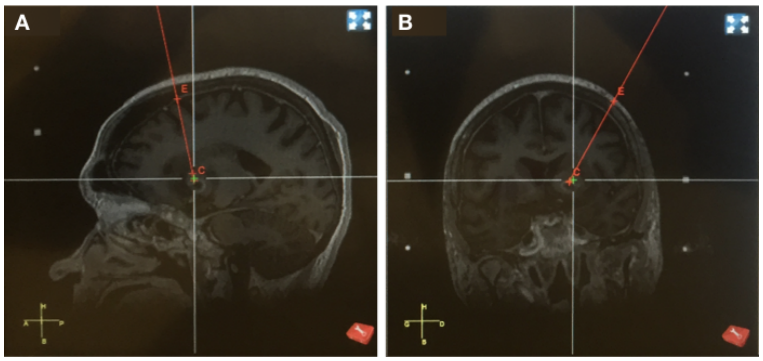

FIGURE 1 Deep biopsy: sagittal view (A), coronal view (B)

Localisation, Medical devices, Surgical navigation, Surgical robots, Tracking systems, Intrabody localisation

1 | INTRODUCTION

Today, surgeons only have few possibilities and still unprecise tools to reach deep and essential structures in the human body. In neurosurgery several emerging therapies as deep brain stimulation (Hariz et al., 2013) and gene therapies (Hocquemiller et al., 2016) constrain to operate in deep brain zones, reinforcing such need. The real medical challenge consists in reaching deep pathological structures (Figure 1) without lesioning important areas of the brain. Indeed, key functional connections and feeding vessels are located between the cortex surface and the potential target which may possibly be deeply located in the brain as white matter tracts showed in Figure 2. Nowadays, neurosurgery interventions are based on precise imaging modalities like CT (Computerized Tomography) scans and MRI (Magnetic Resonance Imaging), providing sub-millimetre pre-planned path (Fitzpatrick, 2010; Lu et al., 2015). These systems, while producing a precise spatial resolution, may not be used as real-time tools (not sufficient temporal resolution), possibly lowering the precision of the surgical intervention, as the brain may shift with cerebrospinal fluid leak or tumour progressive removal. The aim of modern intraoperative neuroimaging is to ensure both spatial and temporal resolution without loosing any accuracy during the surgery.

Advances in microrobotics during the last twenty years (Chaillet and Stéphane, 2013), especially in the propulsion and navigation (Kummer et al., 2010; Khalil et al., 2014; Tottori et al., 2011; Kim et al., 2016; Qiu et al., 2015; Ahmed et al., 2016; Villangca et al., 2016; Dai et al., 2016; Solovev et al., 2009; Magdanz et al., 2015), opened to new perspectives. Navigation inside the human body (Rich et al., 2018; Taylor et al., 2016; Chen et al., 2018), to become fully controllable, needs a tracking system able to provide localisation measurements through tissue and bone layers without injuring the body (Figure 3). To date, studies on microdevice navigation have bypassed the problem by testing in vitro systems and relying on vision based techniques, which are useless in *in vivo* essays (Oulmas et al., 2018; Khalil et al., 2014, 2018). Successive layers of body tissues (Figure 3), through their strongly different characteristics, may therefore bring a lot of perturbations. The challenge is to extemporaneously localise during the surgical procedure a sub-millimetre medical device while keeping the same accuracy even under these perturbations (Mariana Medina-Sànchez and Oliver G. Schmidt, 2017).

In this context, such a system should satisfy several criteria: be safe for humans, be the least invasive, prove the best

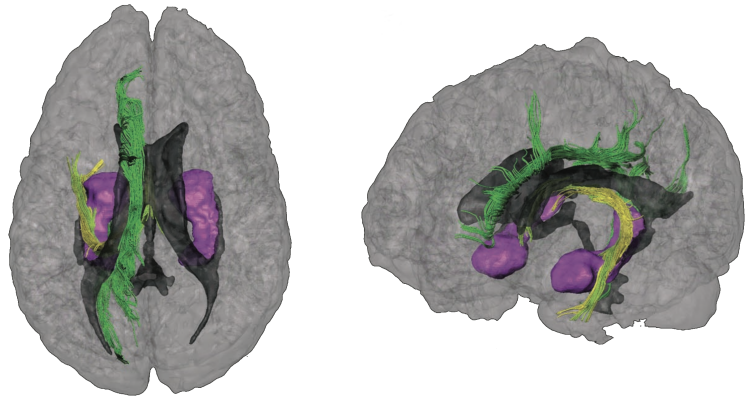

FIGURE 2 3D depictions of limbic system fibers: top view (left), oblique view (right). Figure reproduced from (Wakana et al., 2004)

sub-millimetre localisation accuracy, be able to operate inside the whole head, work in real time, be as small as possible and consume the minimum amount of energy.

As for the multi-dimensional challenge of intracranial localisation, the present paper aims to provide the state of the art of medical device tracking systems. The study covers the different solutions for intra-body localisation and highlights consequences and challenges of the intracranial situation. The contribution of this work consists in mixing head environment conditions and microdevice localisation requirements.

Systems will be classified by underlying physical principle. For each system, physics and the possible localisation measurements are deeply described to then highlight their limits concerning needed therapies.

2 | EXISTING TRACKING SYSTEMS

The literature on tracking systems for human body leads to a physical classification: magnetic field (2.1); electromagnetic waves (2.2) based on their frequencies (radio (2.2.1), optical (2.2.2), and very high (2.2.3)); magnetic resonance (2.3); ultrasound waves (2.4) separated in imaging (2.4.1) and tracking systems (2.4.2); and hybrid systems (2.5). Physical effects and characteristics of the biological environment are presented to better explain the strengths and weaknesses of each technology. Afterwards, the different systems and their features are detailed, to later propose evolutions needed to attain the intraoperative tracking of a micro-medical device in the head.

2.1 | Magnetic field

In (Feynman, 1963), Feynman demonstrates that both magnets and coils[1] generate the same field shape. The papers presented in the current section are based on one of these two components. According to (Feynman, 1963), the magnetic field at a certain point may be expressed along the three dimensions: B_x, B_y and B_z. When considering the distance ratios it is clear that $B \propto \frac{1}{R^3}$, i.e. the magnetic field proportionally decreases with the inverse of the cubic distance.

From a biological point of view, the human brain is a multi-layered heterogeneous structure with different relative

[1] The only condition for the coil to generate the same field shape is the geometry ratio between the current loop and the distance coil - measuring point which has to be small enough.

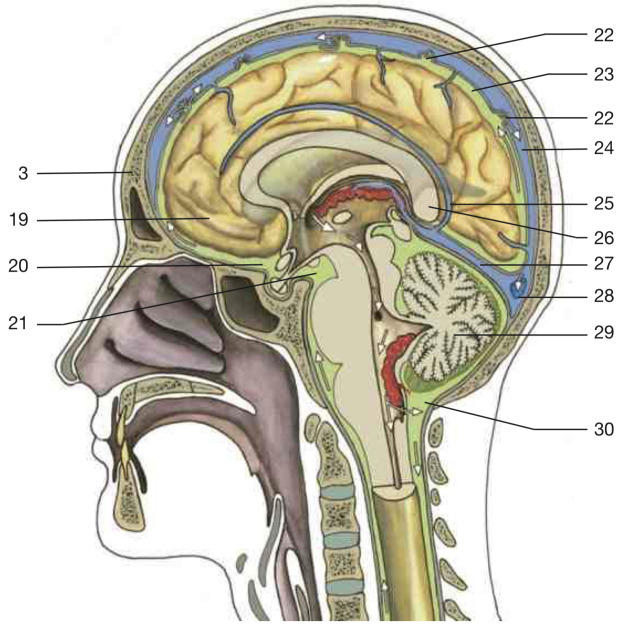

FIGURE 3 Head anatomy. Figure reproduced from (Rohen et al., 1998)

permittivities ϵ_r. Michel, Hernandez and Lee (Michel et al., 2017) provide specific values for brain mediums and demonstrate that water concentration levels result in different permittivities. Indeed, the electrical characteristics of the water molecule and, consequently, the relative permittivity of the medium is function of the wave frequency. Figure 4 illustrates the electrical behaviour of brain tissues versus wave frequencies (data source: (Hasgall et al., 2018)). It appears that the relative permittivities of the gray and white matters drastically fall above $10Hz$ directly impacting the magnetic field (**??**).

The authors of (Son et al., 2016) propose a tracking system that consists of an embedded magnet on a medical device ($6.8 \times 6.8 \times 12.4\text{mm}^3$) powered by an external magnet and whose position is acquired through an array of 64 Hall-effect sensors[2] (Figure 5). Each one measures the magnetic field B (**??**). The system is able to measure both position and orientation of a device with an accuracy of 2.1mm and 6.7° at a frequency of 200Hz and a depth of 50mm. Moreover, a magnet has to be embedded in the device but it doesn't need an energy source. The system may be considered as mini-invasive, since a millimetric incision is sufficient for its insertion.

(Plotkin and Paperno, 2003) describes a tracking system based on a 64-coil array and an embedded, monoaxial receiving coil (0.9mm in diameter and 3mm in length) (Figure 6). To ensure the best trade-off between accuracy and tracking frequency, the authors separated the process in two steps: the initialization consists of sequential activation of the 64 coils to maximize the accuracy, whereas the tracking step uses only a subarray of 8 coils to reduce the computation time. This technology ensures a sub-millimetric position accuracy ($750\mu m$) and 0.7° orientation accuracy at $50Hz$ and up to $200mm$ in depth. The embedded coil is bulky and an energy source is needed to treat the signal received by

[2] A transducer whose output voltage varies with the magnetic field. It allows to measure electrically the magnetic field.

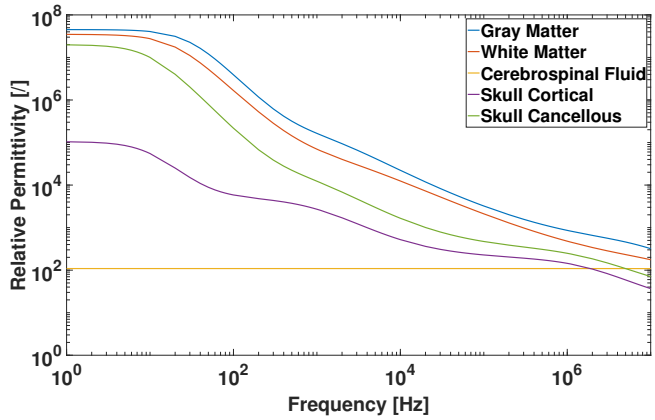

FIGURE 4 Relative permittivity of tissues versus waves frequency (curve plotted with data from (Hasgall et al., 2018))

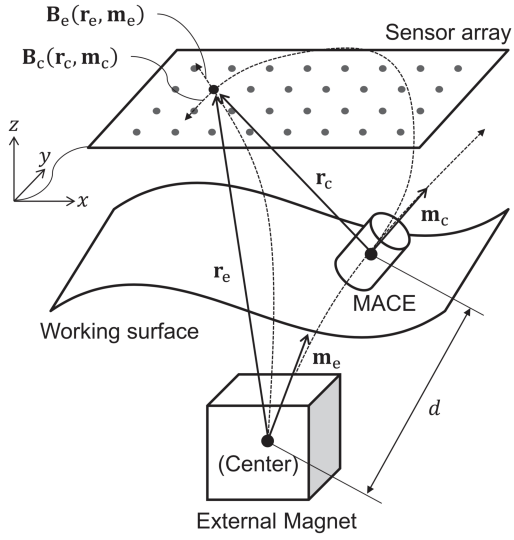

FIGURE 5 Tracking system proposed by Son et al. Figure reproduced from (Son et al., 2016)

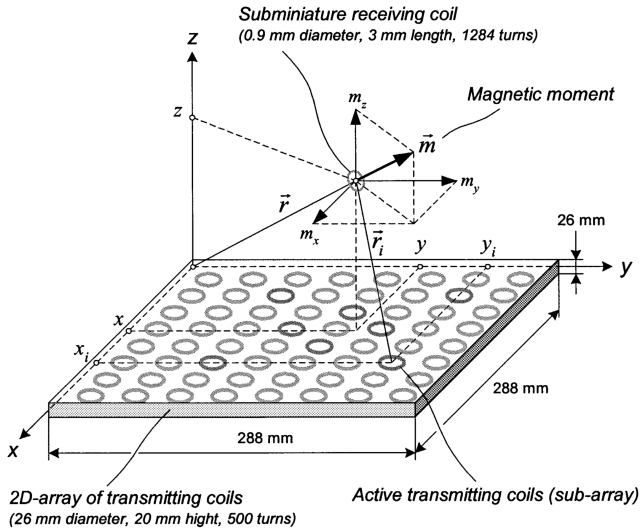

FIGURE 6 Tracking system proposed by Plotkin and Paperno. Figure reproduced from (Plotkin and Paperno, 2003)

the coil. The millimetric dimensions of the coil allow to classify the system as mini-invasive.

Another system, proposed in (Dai et al., 2018), relies on a three-axes embedded magnetometer which measures both an alternating magnetic field generated by an external coil to obtain the position and the geomagnetic field to get the orientation (see Figure 7). This sensor technology guarantees an accuracy of 1.3mm and 1.4° up to 2500Hz and 100mm depth. The embedded sensor needs energy to work and $3 \times 3 \times 1.4\text{mm}^3$ onboard being therefore considered as mini-invasive. The results were obtained in an open-space environment and are therefore not completely applicable for an intra-body evaluation.

The last tracking system of this section is an external rotating magnet driving a spiral motion of a capsule (Kim et al., 2010). It is equipped with 4 Hall-effect sensors (2 on the rotation axis and 1 on each other axis) mounted on a structure of $5 \times 5 \times 5\text{mm}^3$, classifying the system as mini-invasive. The peaks in the magnetic field, which appear when the sensors are aligned with the field, allow to determine the position and orientation of the capsule. The authors show position and orientation accuracies of about 10mm and 8°, respectively, for a maximum distance of 300mm. The working frequency was not specified in their paper.

The millimetric dimensions needed to embed one of these four systems does not meet the bulkiness requirements of a micro-medical device. Usually, sensor downsizing worsens the Signal to Noise Ratio (SNR), degrading the system accuracy. The SNR of magnetic sensors, being proportional to their dimension, limits them around the millimetre because of the noise generated by the brain (Hämäläinen et al., 1993). The challenge consists therefore in reducing the system size while maintaining the SNR. In addition, the results presented by the different authors were obtained in homogeneous environments while the human head is composed of several mediums which would probably alter the signals and decrease the declared performance. Magnet-based devices also suffer from environmental magnetic noise coming from different sources (geomagnetic field, surgical instruments, imaging systems, persons, far environment like subway or tram). The problem might be mitigated by introducing a Faraday cage for shielding purposes. To conclude, (**??**) clearly highlights the link between the signal strength and the inverse of the cubic distance travelled, creating a physical barrier that is still difficult to bypass.

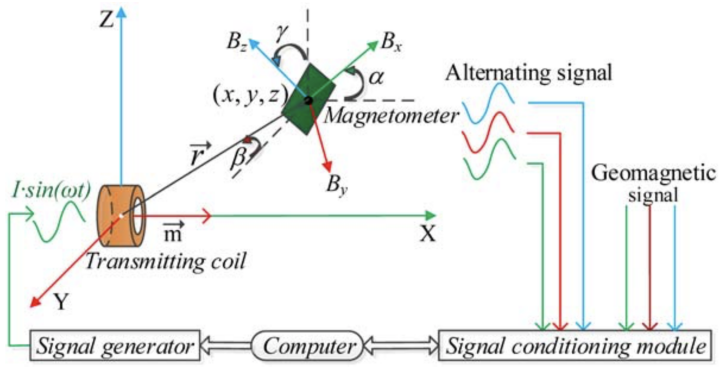

FIGURE 7 Tracking system proposed by Dai et al. Figure reproduced from (Dai et al., 2018)

2.2 | Electromagnetic waves

An electromagnetic (EM) signal sent by an embedded medical device to a sensor, through a medium, may be expressed through the wave theory:

$$r(t) = PL(d)\, s(t - \tau_d(\omega)) + n(t) \tag{1}$$

being $r(t)$ the received signal at time t, $PL(d)$ the path loss coefficient along the distance d, $s(t - \tau_d(\omega))$ the signal sent at time $t - \tau_d(\omega)$, $\tau_d(\omega)$ the delay of the wave propagation at the pulsation ω and $n(t)$ the total noise. The norm of the noiseless signal may be defined as in (2) with initial intensity I_0 and absorption coefficient α. The latter may be linked to the imaginary refractive index of the material κ and the wavelength λ (3) (Saleh and Teich, 2001).

$$|r(t)| = |s(t - \tau_d(\omega))| PL(d) = \sqrt{I_0} e^{-\frac{\alpha}{2} d} \tag{2}$$

$$\alpha = \frac{4\pi}{\lambda} \kappa \tag{3}$$

The delay in the wave propagation $\tau_d(\omega)$ is:

$$\tau_d(\omega) = \frac{d}{\bar{v}_d(\omega)} \tag{4}$$

with $\bar{v}_d(\omega)$ the average velocity along the path d modeled in (Kawasaki and Kohno, 2009):

$$\bar{v}_d(\omega) = \frac{c}{\sqrt{\epsilon_r(\omega)}} \tag{5}$$

being c the speed of light in vacuum and $\epsilon_r(\omega)$ the weighted average of the tissue relative permittivity along the path d at the pulsation ω. The relation between the wave pulsation ω and the tissue relative permittivity ϵ_r is explained in section 2.1 Figure 4. The phase of the EM signal is not proportional to the distance, not allowing a direct link between signal and travelled distance. An EM signal may also be described according to the quantum theory, as a particle, the

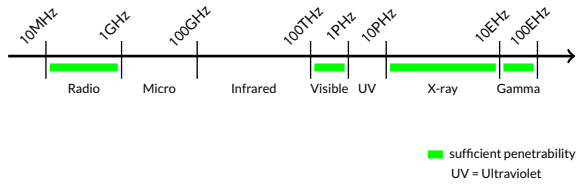

FIGURE 8 EM spectrum (data from (Than et al., 2012))

photon, whose energy is expressed in (6).

$$E = \hbar f = \frac{\hbar c}{\lambda} \tag{6}$$

where $\hbar$ is the Planck's constant, f the photon frequency, λ its wavelength and c the speed of light in vacuum.
The EM spectrum is split into frequency-wise families (Figure 8). The authors of (Than et al., 2012) mention that only radio, optical, X-ray and gamma frequencies show a sufficient penetration power in human tissues. Yet, no complete study on human tissues absorption has been conducted; in other words their imaginary refractive index κ is not completely known. Nevertheless, a few works on narrow spectra have been published, as the representation of the effective depth of magnetic field penetration for half of the radio frequencies [10MHz – 500MHz] (Figure 9) (Röschmann, 1987); the measurement of the refractive index of the skin epidermis and dermis for the visible spectrum [187THz – 999THz] (Ding et al., 2006); or the energy absorption buildup factor of different tissues for the very high frequencies [2EHz – 480EHz] (Manohara et al., 2011). The head multi-tissue structure creates reflections at interfaces, which directly impact the localisation measurement by creating fake positions (Figure 10) (Pourhomayoun et al., 2014). Tracking systems will be discussed by dividing them into three subfamilies with sufficient penetrability: radio, optical and very high frequencies (X-ray and gamma ray).

2.2.1 | Radio frequencies

For the Radio Frequencies (RF) range, the path loss coefficient $PL(d)$ (1) of the signal propagation in the human tissues is statistically modeled in (Sayrafian-Pour et al., 2009) (7).

$$PL(d) = PL(d_0) + 10\alpha log_{10}(d/d_0) + S,\ d \geq d_0 \tag{7}$$

where $PL(d_0)$ is the path loss at the reference distance $d_0 = 50mm$, α the path loss exponent and S the random scatter caused by the multiple materials environment. The authors provide $PL(d_0)$, α and S for deep and near surface tissues which are only valid for a distance d greater than the d_0 threshold (Sayrafian-Pour et al., 2009). Their work bypasses the lack of refractive index values for radio frequencies.

The authors of (Pourhomayoun et al., 2014) propose a tracking system based on a RF sensor grid outside of the body working with an embedded medical device which emits EM waves. Their work is based on (1) which considers the phase shift and the path loss. Figure 11 shows the system principle with sensors on the body skin and a grid at the bottom. The sensors acquire the signal sent by the implant and the processing unit compares it with a model to deduce

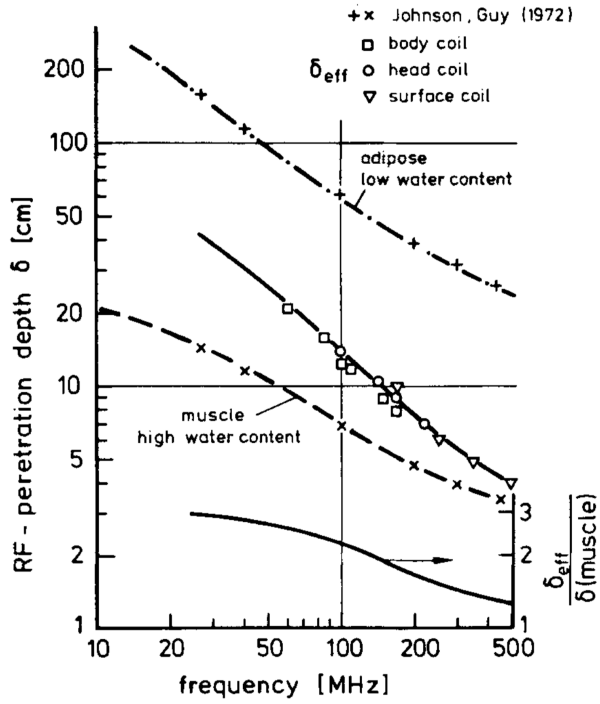

FIGURE 9 Effective penetration depth of electromagnetic waves in human body. Figure reproduced from (Röschmann, 1987)

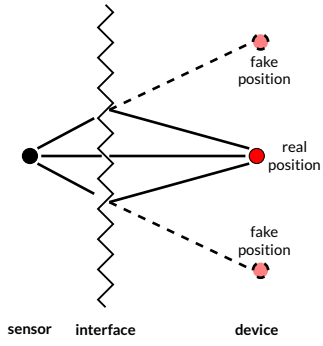

FIGURE 10 Multi-path situation in a localisation process

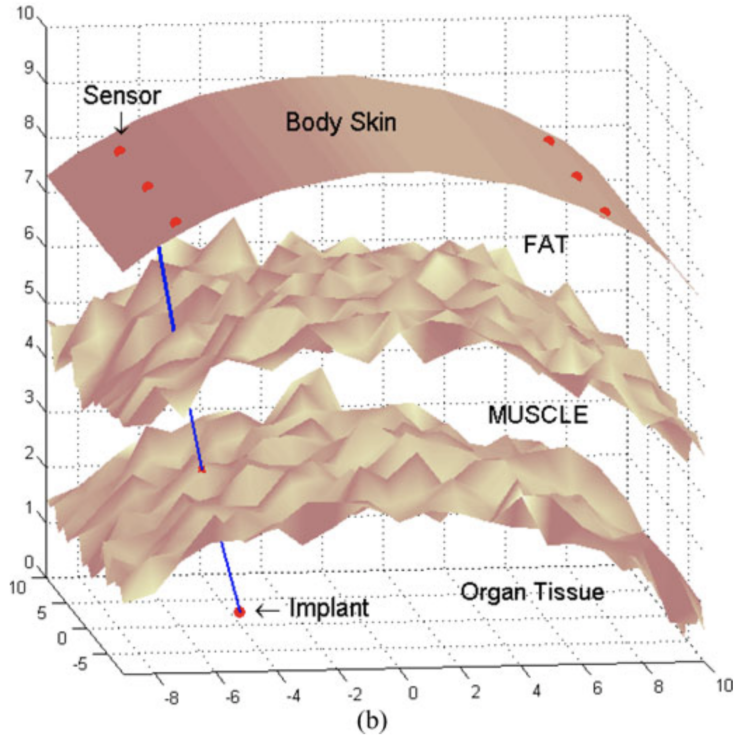

FIGURE 11 Tracking system proposed by Pourhomayoun et al. Figure reproduced from (Pourhomayoun et al., 2014)

the implant position. This method constitutes a trade-off between the grid step and the computation time. In simulation, they achieved a position accuracy of 7mm from 50mm to 100mm deep but the potential operation frequency was not specified. If used for capsule endoscopy, such system could be considered as mini-invasive or invasive, depending of the capsule size. In addition, the emitter needs onboard volume and energy to operate.

Another RF system is based only on the path loss equation (7) (Wang et al., 2011). The authors built a system of one or two grid(s) of 4×4 sensors placed on the body surface and paired with an embedded RF emitting capsule. They directly deduce the distance from the received signal strength (RSS) and neglect the delay created by the different body layers. In simulation, they reached, for 3 organs (stomach, small and large intestines), a position accuracy of 40mm for a depth going from 50mm to 200mm. They don't specify the operational frequency; their embedded capsule is bulky and uses energy to send the localisation signal. The capsule endoscope may be classified, depending on its size, as mini-invasive or invasive.

The authors of (Wille et al., 2011) introduce a RF tracking system based on phase difference thanks to the Radio Frequency IDentification (RFID) process[3]. They placed several RFID sensors around a tank simulating the human body and inserted a RFID tag ($90 \times 10 \times 1\text{mm}^3$) which ranks the system as invasive. The authors trained the system at different known positions to find the optimized measurement sensor weights in the tag working space. With their fine grid training (5mm step), they achieved a position accuracy of 1.6mm for a depth between 85mm and 117mm. The orientation

[3] see page 15 of (Li, 2012) for details on localisation with RFID.

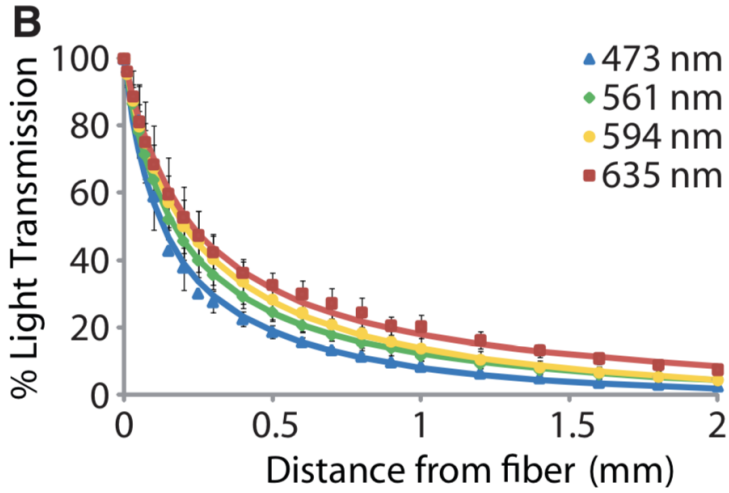

FIGURE 12 Study by Yizhar et al. about light penetration in brain tissues. Figure reproduced from (Yizhar et al., 2011)

of the tag didn't change during the experiment and the operational frequency isn't mentioned. The tag does not use energy to work but needs its volume to be embarked.

The millimetric (or more) dimensions needed to use the presented RF devices do not correspond to micro-medical devices requirements. Furthermore, the results were obtained via simulations or in homogeneous environments, limiting their relevance. Indeed, the cranial space would impose to increase the invasiveness by creating a window in the skull to maintain the performance or to reduce the accuracy by going through the layers. Concerning the noise, the EM frequencies regulation reserves a specific frequency band for each EM communication family reducing any noise-related issues. Finally, the main limitation of EM RF techniques is their lack of accurate human body modelisation.

2.2.2 | Optical frequencies

Optical signals have a low penetration depth in comparison to the RF signals. In the supplementary methods section of (Huber et al., 2008), the light penetration inside a murin opened brain is depicted, showing that the light intensity is halved after one millimetre propagation. The authors of (Yizhar et al., 2011) measured the light penetration inside brain tissues as well, and found a penetration depth capped to 2mm (Figure 12). In the case of closed skull, the light would not penetrate inside the brain due to the total absorption of the light by the bone layer. This phenomenon strongly reduces the applications of the optical frequencies and limit them at close environment localisation.

A pertinent work on such approach was proposed in (Bao et al., 2014) and consisted of a Wireless Capsule Endoscope (WCE) equipped with a 6 frames per second (fps) camera for non-invasive imaging of the gastrointestinal (GI) tract. The authors proposed an odometry process which uses an ASIFT[4] feature points recognition algorithm. As

[4] More details about Affine Scale-Invariant Feature Transform (ASIFT) can be found in (Morel and Yu, 2009).

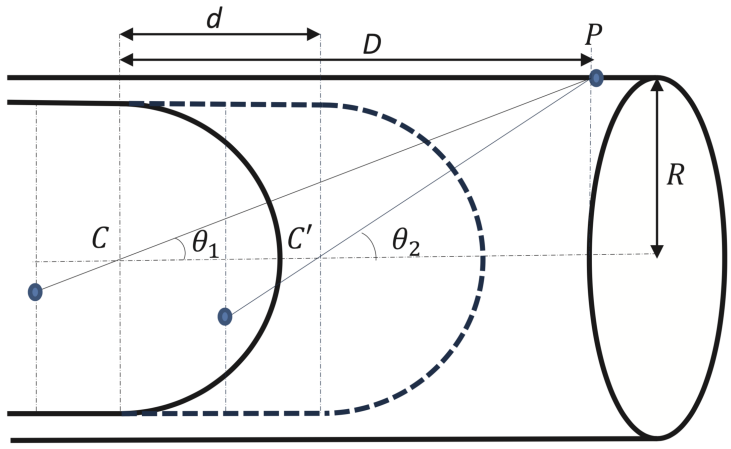

FIGURE 13 Visual odometry schematic proposed by Bao et al. Figure reproduced from (Bao et al., 2014)

illustrated in Figure 13, the displacement between two frames is then estimated through basic geometry, with P the feature point detected in both frames, C and C' both camera positions, θ_1 and θ_2 both angular depths and R the small intestine radius[5]. The authors attained an accuracy of 2.71cm with tests on consecutive couples of frames taken by an endoscope. In a real case, as the estimations of the new pose is based on the previous one, uncertainty on the actual localisation would grow at each new pose estimation. This type of localisation system (i.e. relative) regularly needs an accessory absolute localisation system to correct the position and then avoid the divergence of the error. As accuracy was extrapolated only on couples of adjacent frames, it cannot be compared in a longer frame time, i.e. $\frac{2}{6}$s. The system operates at 6Hz and is considered as invasive because of the camera embedded which needs onboard volume and energy to work. In conclusion, the optical waves, as strongly attenuated by the brain, need to be embarked inside the device. Nevertheless, the current technologies (mainly points recognition) are not competitive and need to be improved.

2.2.3 | Very High frequencies

As explained in (6) the higher the frequency, the higher the photon energy. Very High Frequencies (VHF) gather the photons able to ionize[6] an atom. The absorbed dose by the human body during an exposure of such radiations is measured in Gray (Gy) which corresponds to one Joule absorbed per kilogram of matter. The harmfulness of the dose is measured in Sievert (Sv) and depends on the tissues sensitivity and radiation type. According to the World Health Organization (WHO) the exposure to such radiations may cause organ malfunction or effects such as skin redness, hair loss, radiation burn or acute radiation syndrome (WHO, 2016). In such context, the International Commission on Radiological Protection (ICRP) recommends exposure dose limits to avoid adverse health effects (Table 1) (Valentin and on Radiological Protection, 2007).

[5] The authors published an algorithm which automatically computes the small intestine radius R (Liang Mi et al., 2014).

[6] A photon (or an already pulled out electron), classified as an ionizing radiation, hits an atom and pulls out an electron resulting in an ion creation or in other words, an electron-hole pair generation. It is called the photoelectric effect.

[7] Exposure of workers incurred as a result of their work.

	Limit dose from occupational exposure[7]	Limit dose from public exposure
Effective dose	20mSv/year, averaged over 5 years, no single year > 50mSv	1mSv/year

TABLE 1 Limit doses recommended by ICRP (data from (Valentin and on Radiological Protection, 2007))

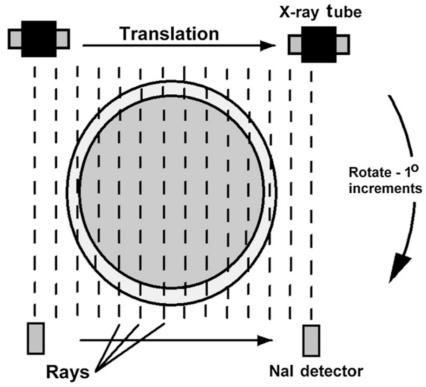

FIGURE 14 Slice imaging principle of a CT scanner. Figure reproduced from (Goldman, 2007)

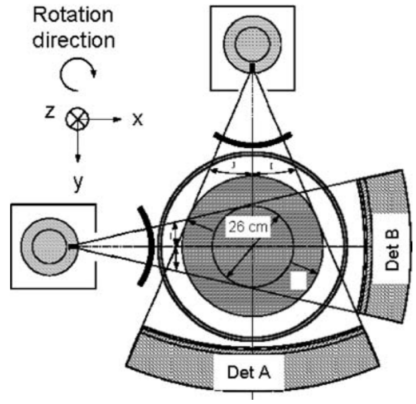

FIGURE 15 Principle of a dual-source CT. Figure reproduced from (Flohr et al., 2006)

The CT scanner consists of an X-ray tube[8] coupled to a scintillation detector[9], mounted face-to-face on a rotating gantry (Goldman, 2007). CT scans provide image slices of the target organ by pre-planned translation and rotation of the sensor array (Figure 14). This technology does not need to insert anything in the human body, and is therefore totally non-invasive. As for performances, the advantage of a 64-slice sensor instead of a 16-slice was demonstrated in (Flohr et al., 2004). The larger number of slice, combined to an advanced z-sampling[10] technique, allows to obtain thinner slices along the z-axis and results in $0.36 \times 0.36 \times 0.36\text{mm}^3$ voxels with temporal resolution between 160ms and 85ms, i.e. 6.3Hz and 11.7Hz. The authors of (Flohr et al., 2006) also evaluated a dual-source CT scanner constituted of two tube-detector couples (DSCT) with a relative angular offset of 90° on the gantry (Figure 15). This structure allows to half the slice time if compared with the simple source CT scanner. The authors achieved a voxel size of $0.5 \times 0.4 \times 0.4\text{mm}^3$ with a temporal resolution of 83ms, i.e 12Hz. The CT technology needs neither energy source nor volume onboard because of its noninvasiveness.

The Positron Emission Tomography (PET) scanner is based on radioactive molecules whose decay releases photons detected by scintillation detectors. The main used radiotracers and the medical aspects of such systems are detailed in (Shevzov-Zebrun et al., 2015). The performance of the PET technology was theoretically studied in terms of spatial

[8] Vacuum tube composed of a cathode, emitting the electrons, and an anode, collecting the electrons. The collision of the electrons with the anode material creates an energy radiation, usually perpendicular to the path of the electrons, as X-rays.

[9] Scintillator (luminescent material which re-emits the absorbed energy in the form of light) coupled with an electronic light element which transforms the light in an electric charge.

[10] By convention z axis is perpendicular to the 2D images.

resolution (Moses, 2011). The author obtained a theoretical maximum spatial resolution of 2.36mm FWHM[11] for a clinical camera. PET technology only needs the volume to embark radiotracers whose size ranks the technology in the micro-invasive family.

Both CT and PET scans, considering their performances and constraints, fit micro-medical device requirements. The major limit of such technologies is the potential for causing harm associated to an elevated exposure to high frequencies waves. A link between exposure and lifetime attributable risk of cancer incidence was demonstrated in (Huang et al., 2009). This effect leads to limited doses or, in other words, maximum operation time imposed by regulators, blocking their use for long-time applications.

2.3 | Magnetic resonance

MRI uses signals emitted by mobile hydrogen (protons) within the human body. Indeed, their spin, because of their electric charge, generates a detectable magnetic field. An MRI measurement is comprised of three steps:

- A superconductive magnet creates a stationary external magnetic field which causes a few mobile protons per million to align and reach a low energy state.
- Transmit coils generate RF radiations (perpendicular to the magnet magnetic field) absorbed by the protons which consequently jump into a transient higher state. The 2D space (slice) is coded by the amplitude and phase of RF radiations.
- After RF radiations stop, protons relax and emit photons at their resonance frequency. The relaxation time constants are measured to obtain MRI images.

MRI domain is based on three main techniques:

- T1-weighted imaging measures the time taken by protons to relax, i.e. the time taken to return to the lower energy state. This process needs an energy exchange between the protons and their environment, in other words the macromolecular environment is indirectly measured.
- T2-weighted imaging measures the decay of the protons signal resulting in cumulative losses in phase coherence due to the protons dephasing. The duration of this phenomenon reflects the proportion of mobile hydrogen, typical of a specific tissue.
- Proton density (PD) measures the signal of mobile protons proportion by minimizing the T1-weighting and T2-weighting signals.

For more information, MRI sequences, equipment and clinical use are detailed in (Himes and Young, 2015).

The settings used in the study on ultra-high resolution brain images (Zeineh et al., 2014) are listed in Table 2. Another work (Stucht et al., 2015) introduced a system, correcting the motion of the patient during the imaging time, which achieved high spatial resolution (Figure 16). The settings used for this study are summarized in Table 2 as well.

The MRI technology allows non-invasive imaging of the human body. It respects the requirements for a micro-medical device, in terms of spatial resolution. Table 2 shows time per slice longer than one second, with imaging frequency less than 1Hz. Figure 17 presents the data of Table 2 and highlights a trade-off between spatial and time

[11] Full Width Half Maximum (FWHM) is the width of a spectrum curve at 50% of its maximum. For an imaging system, it corresponds approximately at the minimum distance between two separable objects, i.e. the resolution.

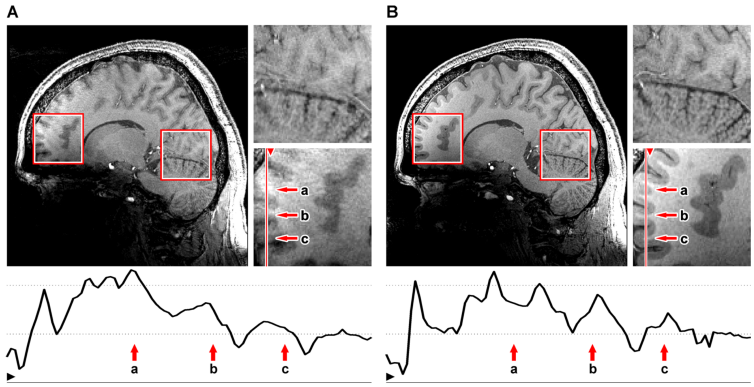

FIGURE 16 0.44mm isotropic voxel with motion correction off (A) and on (B). Figure reproduced from (Stucht et al., 2015)

Voxel size $[mm^3]$	Time taken per slice $[s]$
$0.4 \times 0.4 \times 0.4$	5.18
$0.7 \times 0.7 \times 0.7$	2.06
$0.8 \times 0.8 \times 0.8$	2.01
$0.12 \times 0.12 \times 0.6$	145.33
$0.25 \times 0.25 \times 2$	48.75
$0.44 \times 0.44 \times 0.44$	3.16

TABLE 2 Settings used in (Zeineh et al., 2014) (first line) and (Stucht et al., 2015) (second line)

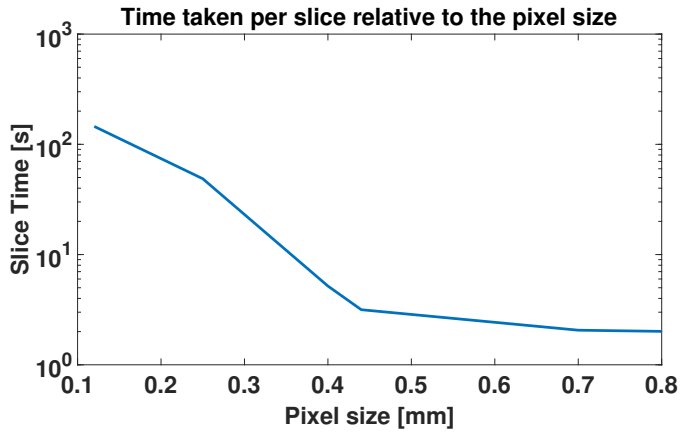

FIGURE 17 MRI trade-off between spatial and time resolution (data from (Zeineh et al., 2014; Stucht et al., 2015))

resolution. In conclusion, with the MRI technology, if sub-millimetric resolution is needed, the time resolution is limited below 1Hz. That is why, so far, the use of MRI technology for sub-millimetre devices tracking has not been implemented.

2.4 | Ultrasound waves

An ultrasound signal travelling through a medium consists of particle vibrations transmitted from one molecule to the next one. Sound waves may be longitudinal or transverse, i.e. particle vibrations may be parallel or transverse to the direction of propagation. Only solids allow transverse sound waves propagation. According to (Ziskin, 1993) soft tissues behave like liquids, i.e. only supporting longitudinal waves, whereas bone can support transverse waves. The sound wave traveling through tissues induces an energy loss due to the internal friction, which is intrinsic to any material. This attenuation includes several processes: the divergence[12], the absorption[13] and the deflection composed of reflection, interfaces refraction, and scattering. The two major sources of attenuation in the human body are the absorption through a tissue and the losses at interfaces.

$$10 \log_{10} \left(\frac{I_r}{I_s} \right) = -A_x \cdot d \cdot f \tag{8}$$

The logarithm absorption $(\frac{I_r}{I_s})$ is linear to the sound wave frequency f in [MHz] and the travelled path d in [cm] with I_r the signal intensity received, I_s the signal intensity sent and A_x the absorption coefficient of the tissue x in [dB/cm/MHz]. Signal loss at the interface is mainly due to reflections caused by differences in the acoustic impedance of the two mediums. Reflection may be specular or diffuse depending on the ratio between interface irregularities and the wavelength. According to (Ziskin, 1993), for human tissues, sound is scattered by cells and tissue elements, because they are small beside the soundwave wavelength. Disturbances are also due to material intrinsic characteristics. The deviation of the transmitted signal is modeled by Snell's law while the Newton-Laplace equation models the speed of sound in a medium.

[12] Effect of spreading the acoustic energy over a larger beam area and therefore reducing the beam intensity.

[13] Effect of transferring the beam energy to the material and degrading it into heat.

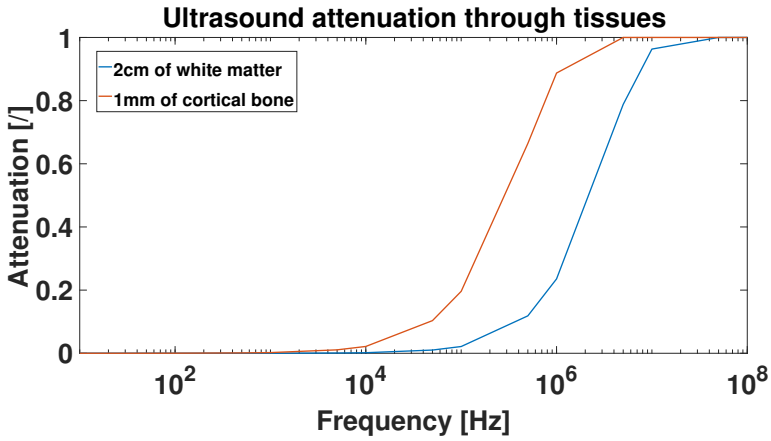

FIGURE 18 Ultrasound attenuation (obtained with 8) for two intra-body path examples (data from (Hasgall et al., 2018))

Concerning the biological environment, the head is composed of several different materials as blood, bone, grey matter, white matter, cerebrospinal fluid (CSF), cerebellum, etc. This diversity causes a lot of reflections along the ultrasound path, like the CSF-grey matter interface reflecting 1.7% of the signal or the cortical bone-CSF transition reflecting 63.1% of the signal (data source: (Hasgall et al., 2018)). These reflections cause multi-path issues and disturb the localisation measurement. In addition, tissues absorption and even more bone absorption are significant. Figure 18 presents the attenuation through the thickness of the frontal A inner table[14] taken from (Lillie et al., 2015) and through 2 cm of white matter relative to the frequency of the ultrasound waves (data source: (Hasgall et al., 2018)). Bone attenuation is twenty times greater than the one due to the white matter.

Ultrasound systems are classified in two subfamilies: on one hand, ultrasound neuroimaging working with acoustic contrast agents inserted in the blood (2.4.1) and on the other hand, ultrasound tracking systems (2.4.2).

2.4.1 | Ultrasound Neuroimaging

Ultrasounds are used to dynamically image the brain by measuring changes in cerebral blood volume (CBV), i.e. the blood flow inside the brain vascular network. The objective is to demonstrate the correlation between an external stimulus and the changed blood flow in the corresponding brain zone. The authors of (Deffieux et al., 2018) give an idea of the phenomenon: the CBV response may occur in one cortical column (approx. 100µm), starts at 0.3s and climbs until 1s after a 300µs stimulus. CBV measurements are realized with power Doppler sequence[15] which, because of the effects mentioned above, lacks of sensitivity to detect small brain elements. The authors explain that acoustic contrast agents (microbubbles) inserted in the blood increase the sensitivity of the system and therefore its resolution. Ultrafast Doppler is another way to boost the SNR and consists in acquiring images at kHz frequencies. According to (Deffieux et al., 2018), skull crossing is still a difficulty but may be bypassed by thinning or opening an ultrasound window through it.

Ultrafast Doppler technology was used to image the thalamus-cortical auditory tract of awake ferrets (Demené

[14] considered as cortical bone

[15] Doppler sequence that measures the ultrasonic energy backscattered from red blood cells in each pixel of the image (Deffieux et al., 2018).

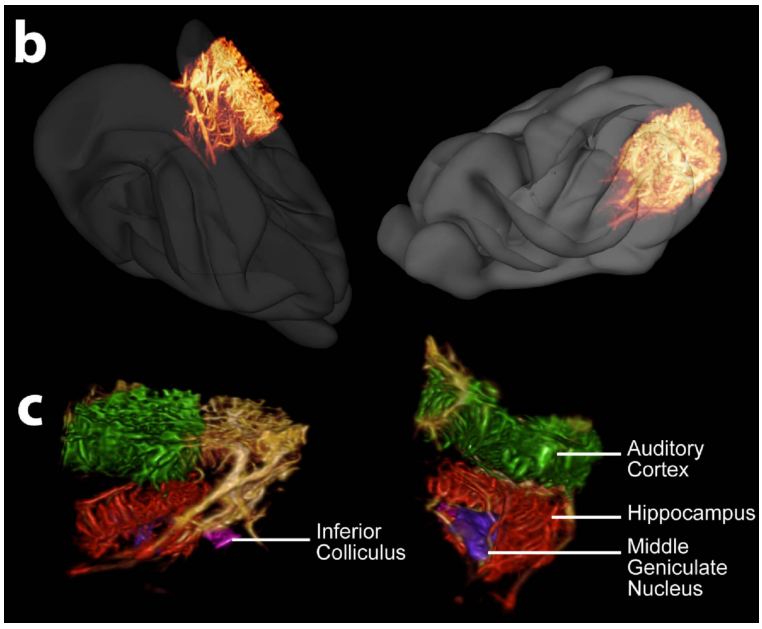

FIGURE 19 Ultrafast Doppler imaging of awake ferrets. Figure reproduced from (Demené et al., 2016a)

et al., 2016a). The authors exploited the UltraFast Doppler Tomography (UFD-T) which briefly consists of 2D power Doppler images acquired at 500Hz (each frame built with 11 tilted plane wave emissions fired at 5500Hz) combined with the translation and rotation of the sensor (for more details, see (Demené et al., 2016b)). They achieved an isotropic 3D resolution of 100µm in a total volume of $14 \times 14 \times 20\text{mm}^3$ (Figure 19). To obtain these results, they performed a craniotomy on each ferret, classifying the method as invasive, and used a custom miniaturized probe with a central frequency of 15MHz.

The ultrafast Ultrasound Localisation Microscopy (uULM) is proposed in (Errico et al., 2015), inspired from the optical localisation microscopy concept (Ehrenberg, 2014), which captures the transient signal decorrelation created by acoustic contrast agents at more than 500Hz. It allows non-invasive sub-wavelength imaging deep in the brain thanks to the breaking of the diffraction barrier. A super-resolved image is constructed by localizing each bubble center separately and accumulating their positions to recover the vessels network, hundred times smaller than the wavelength (Figure 20). The use of microbubbles (with a diameter ranging from 1 to 3µm), thanks to their high deformation, allows to outperform accuracy limitations due to the classical wave diffraction theory which, according to the authors, gives accuracy limits between 200µm and 1mm in clinical applications. In classical ultrasounds, resolution is directly linked to the ultrasound frequency and consequently to the penetration depth (8). In Ultrafast Ultrasound Imaging (UUI), the resolution depends on contrast agents and sensor characteristics: signal-to-noise ratio, bandwidth of backscattered echoes and number of array elements used in the beamforming process which, according to (Errico et al., 2015), give a theoretical resolution of 2.5µm. The authors obtained $10 \times 8\mu\text{m}^2$ pixels, 3mm deep through a thinned skull (invasive method), which corresponds to a ten-times increase in resolution compared to conventional ultrasound imaging. They also performed measurements through the intact skull (non-invasive method) and detected vessels down to 20µm width deeper than 8mm into the brain.

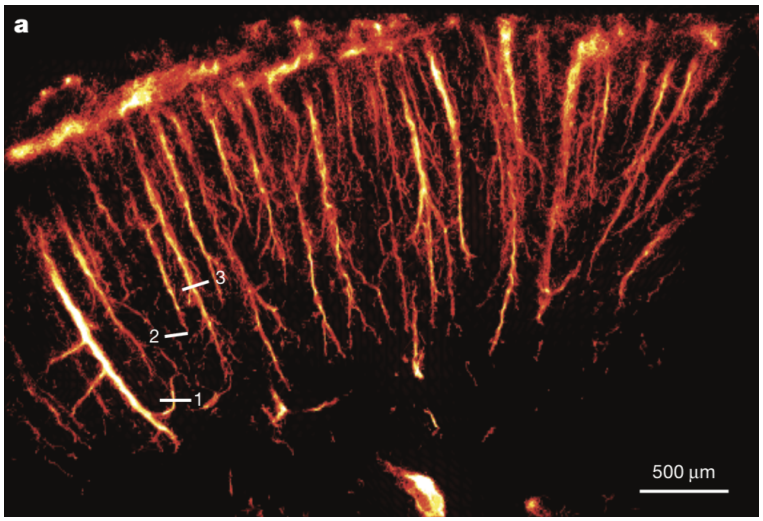

FIGURE 20 uULM realized through a thinned skull with a resolution of 10µm × 8µm. Figure reproduced from (Errico et al., 2015)

2.4.2 | Ultrasound Tracking Systems

Several research teams proposed ultrasound tracking systems which are, here, classified by type of detection: interface reflection (**??**); embarked sensor and bubble use.

The authors of (Gumprecht et al., 2013) built a system consisting of a magnet driving unit and a transcutaneous sonographic probe mounted on a 2D Cartesian robot to, respectively, propel and track the endoscope capsule (15mm in diameter and 38.3mm long) through the back of the patient (Figure 21). The size of the inserted device classifies the system as invasive. The authors tested two measurement processes with phantom gel model of paraffin to simulate the human body:

- measurement of the capsule position, movement of the ultrasound probe with the Cartesian robot, measurement of the new capsule position and comparison of the distance to the reference movement given by the Cartesian robot: the resolution depends on the ultrasound probe;
- centering of the ultrasound probe on a capsule landmark, movement of the capsule thanks to the magnetic drive unit, recentering of the ultrasound probe on the landmark and computation of the probe movement: the resolution depends on the Cartesian robot

They used a commercial probe (2.5-5 MHz center frequency, BK Medical, Herlev, Denmark) with an axial resolution of 2mm and a Cartesian robot having a 1mm movement resolution. With such a setup, they achieved 0.56mm and 0.44mm accuracy for the first and second process, respectively. The working depth was not mentioned in the work.
A closed-loop motion control of paramagnetic microparticles (average diameter of 100µm) using an ultrasound localisation system is proposed in (Khalil et al., 2014). The authors used a commercial ultrasound probe (5.5-18 MHz center frequency, 18L6 HD, Siemens Healthcare, Mountain View, USA), placed at 25mm off the center of the workspace (Figure 22). The calibration of the ultrasound system (with a microscope with an accuracy of 2.34µm per pixel) resulted

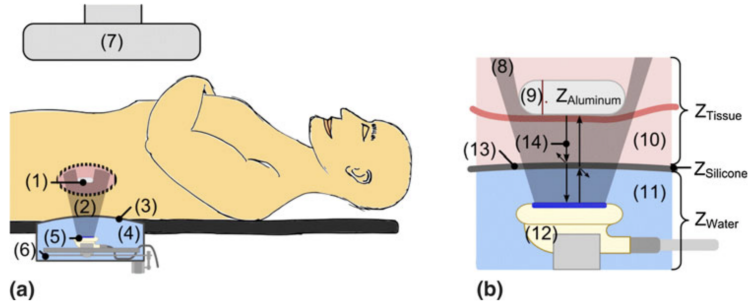

FIGURE 21 (a) Ultrasound robot: (1) endoscope capsule, (2) ultrasound waves, (3) flexible membrane adapting to patient's back, (4) ultrasound liquid, (5) ultrasound probe, (6) kinematics, (7) magnetic drive unit | (b) Layer model: (8) ultrasound waves, (9) endoscope capsule, (10) tissue, (11) ultrasound fluid, (12) sonographic probe, (13) membrane, (14) wave with reflection schematic. Figure reproduced from (Gumprecht et al., 2013)

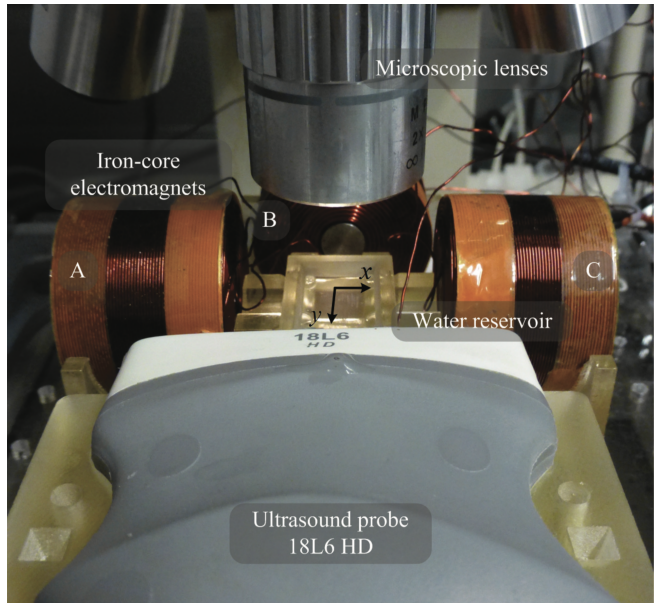

FIGURE 22 Setup with in the center the water reservoir containing the paramagnetic microparticles. Figure reproduced from (Khalil et al., 2014)

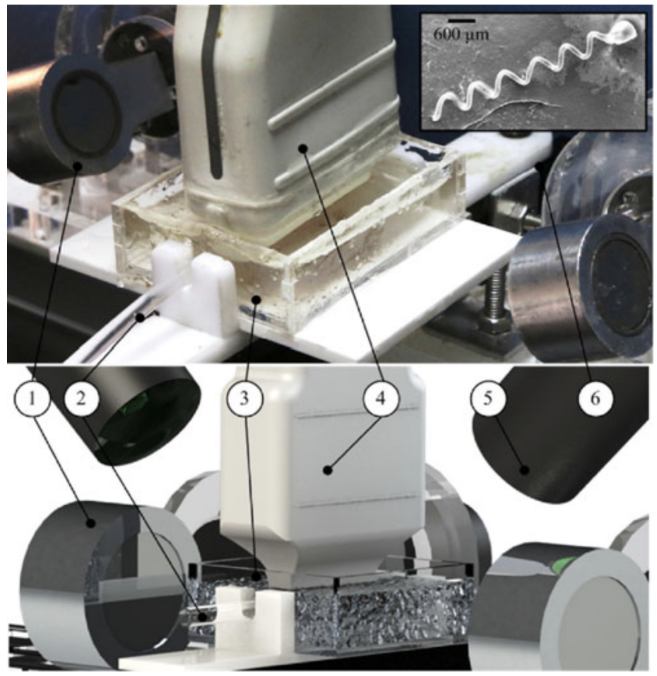

FIGURE 23 Experiments setup of Khalil et al. Figure reproduced from (Khalil et al., 2018)

on a 20.98µm/pixel accuracy with an operating depth up to 35mm. The operating frequency was not mentioned in the paper.

The authors of (Khalil et al., 2018) introduced a new way to rub blood clots with an helical robot, magnetically propelled and using ultrasounds for guidance. As in (Khalil et al., 2014), ultrasound localisation feedback is used to set up a closed loop control and handle the motion of the microrobot (346µm in diameter). The system is composed of the magnetic actuation system (Figure 23:1), microscopes to image the blood clot (Figure 23:5), the ultrasound probe (Figure 23:4) to track the robot, and the testing environment (Figure 23:3) made of gelatin ($6 \times 4.5 \times 1.5 \text{cm}^3$). The authors used a commercial ultrasound system (HD 5 Diagnostic Ultrasound System with transducer NOCTN340, Philips and Neusoft Medical Systems, Amsterdam, The Netherlands) placed 7.5mm away from the catheter segment and set the gain, the frequency and the depth to 43, 10 MHz and 3 cm, respectively. They reached a steady-state error of 0.84mm.

These three systems, as based on wave reflection at the environment-robot interface, need neither volume nor onboard energy to operate. Nevertheless, in-vitro environments are not multi-material and do not produce multi-reflection echoes as the head. Moreover, the ultrasound systems would need a skull window to go through the bone thickness ranking the method as invasive.

A system using embarked sensor, proposed in (Nikolov and Jensen, 2008), consists of an ultrasound probe sending waves to a mini-invasive needle introduced in the patient body and equipped with ultrasound sensors (Figure 24). Sensorized needles allow to avoid specular reflection[16] problems. The authors also suggest another solution: increase the needle surface roughness to generate diffuse reflection. Two measurement processes are evaluated, each based on

[16] Deflection of the sound wave away from the ultrasound probe.

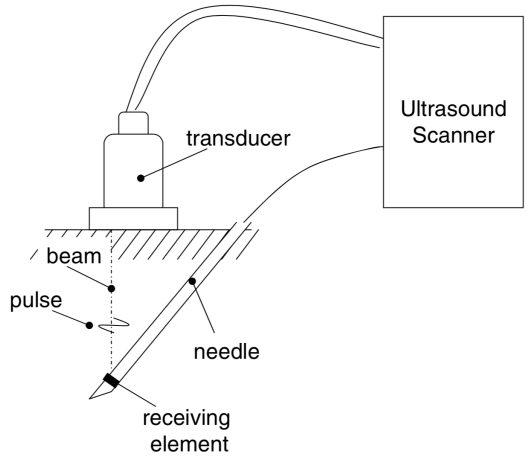

FIGURE 24 Block diagram of the work of Nikolov and Jensen. Figure reproduced from (Nikolov and Jensen, 2008)

the time of arrival:

- the most intense beam received is considered as the most direct sensor on the wave path and then the distance is measured
- the position is found with a classical triangulation algorithm by resolving a linear equation system

Robustness to noise is assured by averaging several position estimates. They used a linear array of 192 US transducers with a center frequency of 7 MHz and with a spacing distance of 202µm. For tip depths varying from 10mm to 120mm, the authors found an accuracy of 0.3mm and 0.1mm, respectively. This system, as sensors are embarked, is bulky and needs energy to operate. Moreover, the authors used a wire to link tip sensors to the processing unit therefore it would necessitate the development of a wireless communication unit onboard to go deeply in organs without wire.

Acoustic reporter genes (ARGs) were recently introduced (Bourdeau et al., 2018) and consist in genetic elements that grant bacteria to be visualized *in vivo* by ultrasounds. According to the authors, these elements are a unique class of gas-filled protein nanostructures, expressed mainly in water-dwelling photosynthetic organisms whose role is their buoyancy regulation. These structures are similar to microbubbles and therefore, allow to outperform the diffraction theory limits, while having a longer lifetime. To demonstrate the concept, they expressed ARGs in E. Coli strain Nissle 1917 (ECN) which is a probiotic microorganism able to colonize the mammalian gastrointestinal tract (Figure 25 and 26). They used a research ultrasound probe (L11-4v128-element linear array transducer, Verasonics) with a center frequency of 6.25 MHz at a depth of 20mm. They attained a detection threshold of 0.005% volume fraction or, in other words, 100 cells per voxel of 100µm side. The system needs onboard volume to embark microorganisms (mini-invasive) but no energy to operate. These results were obtained without going through a bone layer: in that case, a skull window should be required to maintain the accuracy. By being embarked on medical devices, this concept could allow the increase of the accuracy of the ultrasound localisation.

No tracking system (2.4.2) presented in this section proposes a solution to operate through an intact skull. The most

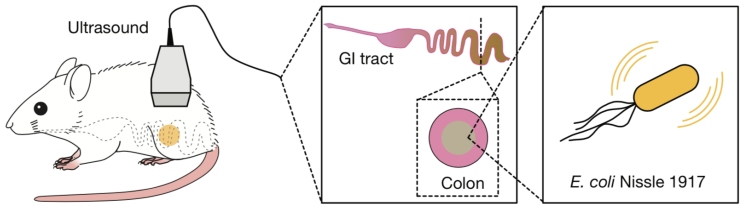

FIGURE 25 Tracking system proposed by Bourdeau et al. Figure reproduced from (Bourdeau et al., 2018)

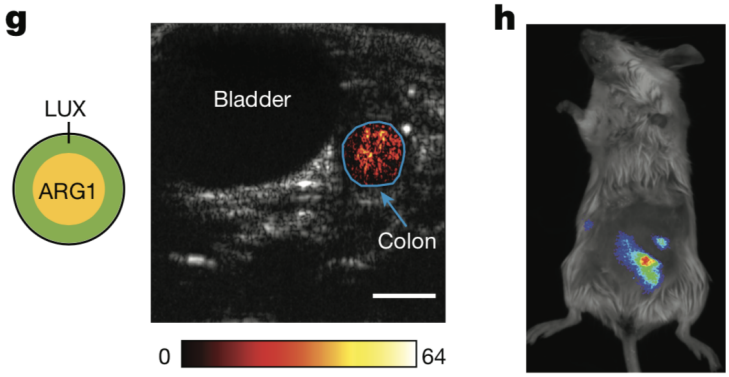

FIGURE 26 Image of acoustic reporter genes inside a murine model. Figure reproduced from (Bourdeau et al., 2018)

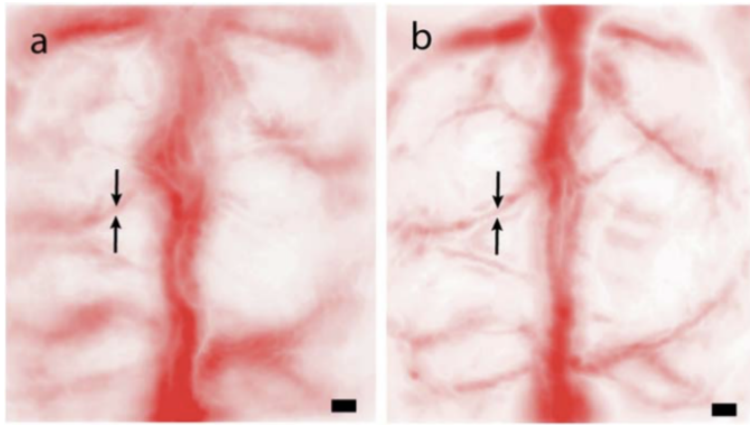

FIGURE 27 Projection views of PAT resolution scans of intact (a) and removed (b) skull. Figure reproduced from (Kneipp et al., 2016)

advanced work on this side is the proposition of ultrasound imaging system in (Errico et al., 2015) where a resolution of 20µm through an intact murine skull is presented. Every proposed ultrasound system fits in terms of volume and energy with micro-medical device requirements. To be fully usable, ultrasound imaging systems (2.4.1) need to be adapted to microdevices, whereas the tracking systems (2.4.2) need to increase their SNR to be able to operate through the skull layer.

2.5 | Hybrid

Hybrid technologies are based on a combination of at least two technologies presented in the previous sections. These types of systems are classified in three groups: photoacoustic; external with internal localisation systems; and combination of imaging principles.

Photoacoustic tomography (PAT), as explained in (Xia et al., 2014), consists of the acoustic detection of the optical absorption of endogenous chromophores[17] or exogenous constrast agent[18]: the energy is sent as light radiations, transformed by human body elements into acoustic energy (photacoustic effect) and detected by acoustic sensors, set outside the body. This technology overcomes the diffusion limit of optical imaging because of the weaker scattering of backward acoustic waves. Distortions, introduced by an adult murine skull in transcranial optoacoustic imaging, are studied in (Kneipp et al., 2016) by comparing intact, thinned and removed skull impact. The skull introduces time shift and ringing artifacts of the optoacoustic signals, limiting the transmission frequency at 5 MHz. The authors obtained a resolution of 40.5µm, 29.4µm and 21.8µm FWHM for the intact, thinned and removed skull, respectively (Figure 27).
The authors of (Buehler et al., 2012) proposed a PAT real-time system for small-sized animal. The machine is based on simultaneous acquisition of signals from 256 points distributed over a spherical surface surrounding the sample and enabling an image region of about $10 \times 10 \times 10\text{mm}^3$ for one laser pulse (Figure 28). To demonstrate the resolution of their system, the authors used a phantom consisting of a 1.9cm diameter light scattering cylinder and containing a

[17] Elements originated from the human body which are responsible of light absorption and consquently of its color. As an example, according to (Young, 1997), the epidermis contains several major solar ultraviolet-radiation-absorbing endogenous chromophores like DNA, amino acids, melanins, ...

[18] Liquid, originated from outside of the human body, intravenously injected into a patient that increases visibility of pathologies, like tumours.

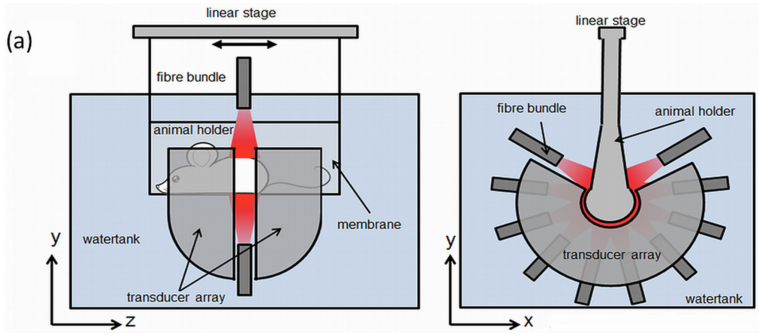

FIGURE 28 Schematic representation of the PAT system proposed by Buehler et al. Figure reproduced from (Buehler et al., 2012)

100µm black absorbing microsphere placed in three positions. The imaging volume is $22 \times 24 \times 3\text{mm}^3$ using voxel of $37 \times 40 \times 40\mu\text{m}^3$. They also performed a test with a murine heart to demonstrate the dynamic imaging of the beating heart. They obtained a transverse and radial resolution of 850µm and 200µm, respectively, at 10 Hz and 10mm depth. This imaging technology requires neither energy nor volume onboard.

Combination of an external and internal localisation system allows to increase the accuracy in comparison to standalone systems. The fusion process, generally based on the error propagation (covariance matrix) of the measurements, is designed to take into account the most precise measurement at each time step. Such a system, proposed in (Goh et al., 2014), uses electromagnetic direction-of-arrival (DOA) and Inertial Measurement Unit (IMU) measurements fused by an unscented Kalman filter (UKF). The authors used their system to measure the localisation and the orientation of a WCE equipped with an IMU and with a transponder to send a localisation signal to the external antennas (Figure 29). Their simulations resulted in a position accuracy of about 3mm for a DOA error of 0.1°. The frequency was not mentioned and the system needs energy for both the IMU and the transponder which are bulky.

Another WCE localisation system, merging embedded visual odometry and RF information, is introduced in (Bao et al., 2015). The algorithm fuses data of the visual odometry (section 2.2.2) (Bao et al., 2014) and of a classical RSS RF architecture based on path loss modelisation (7) with a Kalman filter. It allows the visual motion tracking to avoid cumulative estimation errors leading to drift and to increase the accuracy of the RF measurement (Figure 30). They achieved 5 cm localisation accuracy at 6 frames/sec until approximately 50cm depth. The camera and the RF transmitter need their dimensions in space and energy onboard.

A PET-CT-UUI triple-imaging system which merges the three image modalities for simultaneous co-registered imaging is presented in (Provost et al., 2018). The instrument, composed of commercially available devices, combines the PET millimetre detection of picomolar molecular concentration with the anatomical precise imaging of the CT and with the very high frame rate acquisition of UUI. The imaging volume is $20 \times 12.9 \times 420\text{mm}^3$, which allows to image tumour (Figure 31) with voxel of $400 \times 400 \times 400\mu\text{m}^3$ for PET-CT and $100 \times 100 \times 100\mu\text{m}^3$ for UUI. The registration accuracy achieved is about 95µm but the authors do not precise the operation frequency. The imaging technologies need neither onboard volume nor energy.

The systems proposed in this section demonstrate the same limits of the technologies they combine. The fusion

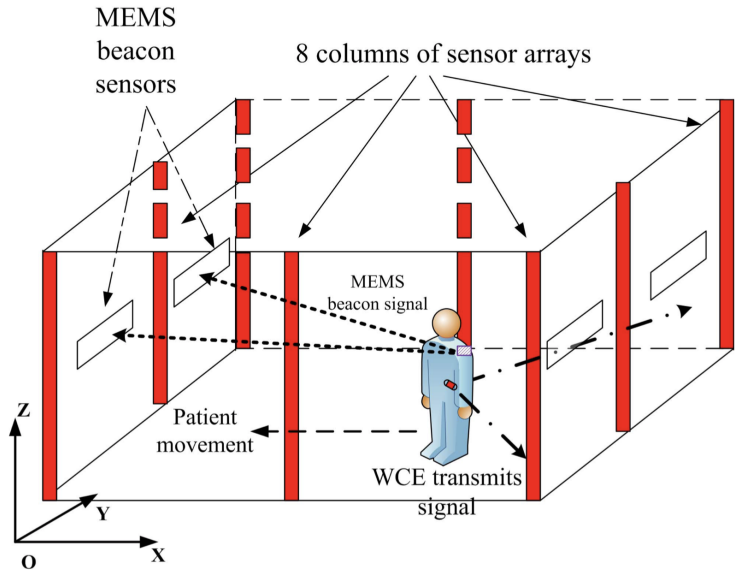

FIGURE 29 Schematic representation of the system proposed by Goh et al. Figure reproduced from (Goh et al., 2014)

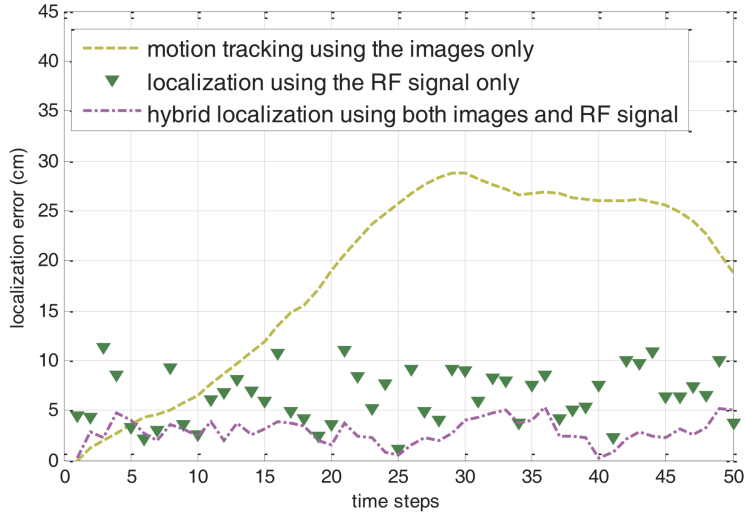

FIGURE 30 Evolution of localisation error as the capsule moves. Figure reproduced from (Bao et al., 2015)

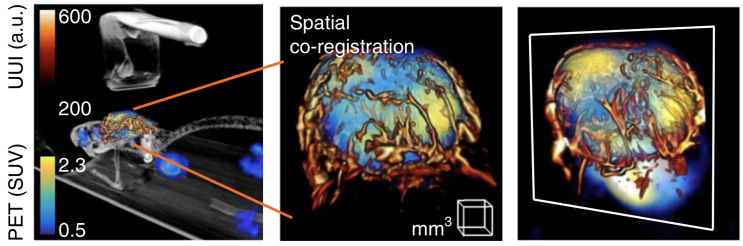

FIGURE 31 PET-CT-UUI images of a mouse tumour xenograft with greyscale for CT, heat scale for UUI, yellow-blue scale for PET. Left: the ultrasound probe located above the targeted tumour in the CT volume and the fused PET– UUI volume depicting the vasculature. Middle: maximal intensity projection view of the spatially co-registered tumour. Right: view of image plane inside the volume. Figure reproduced from (Provost et al., 2018)

algorithm does not totally cancel the cons of each technology but lower them. That is why, the limitations come from the technologies themselves which are not completely ready to be combined and still need intrinsic improvements.

3 | DISCUSSION

Today, during a surgery, practitioners still have to juggle with different localisation and imaging systems. As an example, challenging deep brain tumour to be attained needs a system able to track in real-time a millimetric device to guide it precisely until the operation site. In addition, the already complex medical environment needs localisation systems to be "easy to use", i.e. minimally invasive, reproducible and applicable to patients. This need is particularly highlighted by neurosurgery applications combining tracking means and surgical techniques to reach delivery of novel therapies: Deep Brain Stimulation (DBS) (Hariz et al., 2013); gene therapy or cell grafts (Hocquemiller et al., 2016); tumour improved resection and local delivery of drugs active against tumours (Sanai and Berger, 2008). Figure 32 shows the performance needs of the current and future neurosurgery applications.

For comparative purpose, four quantitative and three qualitative criteria, listed in Table 3, were chosen to represent the main characteristics of each system. The orientation is not taken into account because too few publications address such issue. Figure 33 summarizes all listed systems in 2 by gathering their characteristics through radar diagrams[19]. Each column represents technologies from one family following the architecture of 2. Four colours are used to image the qualitative differences between systems: red: bad health effects; dark blue: the system needs energy **and** volume onboard; blue: the system needs energy **or** volume onboard (only one); light blue: the system needs neither energy nor volume onboard.

For performance comparative purposes, the same solutions are set on a double axes chart (Figure 34): depth and position accuracy are represented on x and y axes, respectively. The frequency is depicted with the shape and the size of the markers: a cross when the system cannot operate in real time, i.e. below 20Hz; and a triangle when the system works in real time, i.e. 20Hz and more. The frequency is mentioned next to the marker when specified by the authors. The colour scale is the same as in Figure 33. Green lines differentiate the zone equivalent to 100% of the scale chosen for comparison (Table 3).

[19] Radar charts are composed of axes pointing towards the exterior of the shape, each one represents one criterium. This representation enables the area to draw a shape whose size depends on the correlation between the system's characteristics and the criteria.

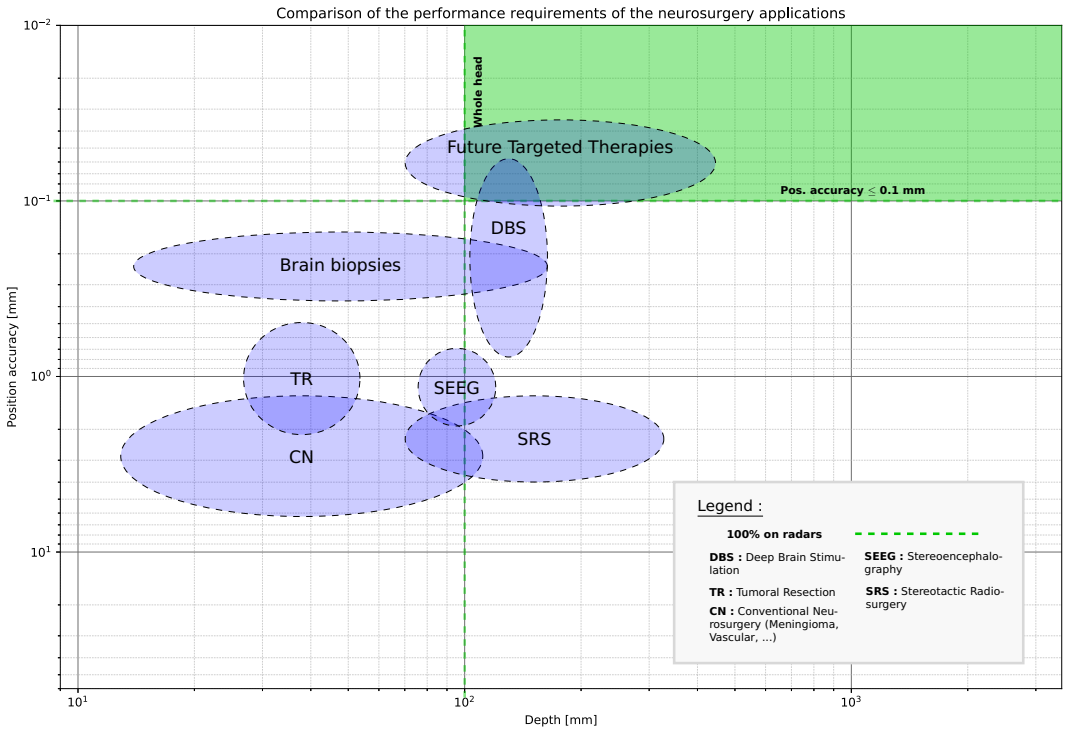

FIGURE 32 Comparison of the performance requirements of the neurosurgery applications

Criterion	0%	100%
Quantitative		
Position accuracy	1 mm, millimetric accuracy	0.1 mm, sub-millimetric accuracy
Depth	0 mm	100 mm, roughly half of the head (Bushby et al., 1992)
Frequency	0 Hz	20 Hz, considered as real time
Non-invasiveness	Invasive (opening > 1cm)	No insertion
Qualitative		
Take volume	Yes	No
Need energy	Yes	No
Bad health effect	Yes	No

TABLE 3 Criteria used to compare the tracking systems

The system distribution lets appear a diagonal line going from the top of the y-axis to the end of the x-axis. In terms of performance, it means that a system cannot satisfy both deep penetration and high resolution. It appears a current three dimensions performance compromise: accuracy-depth-frequency, partly depicted by the limit diagonal.

In addition, the need to be less invasive is brought by both the desire of diminishing side effects on the patient (caused by anesthesia and openings in the skull) and the accuracy requirements. Invasiveness, through its impact on the registration[20] step, caps the reachable accuracy. Indeed, a skull opening, by creating a leak of CSF, induces a brain shift (potentially up to few centimeters) which falses the targeted operation site acquired from pre-operative imaging techniques. The reduction of the invasiveness can be achieved by decreasing the skull opening size or even by not opening it, which induces a skull layer to be crossed. The performance of the localisation system is directly impacted by this layer which increases both the depth and the attenuation along the signal path (Figure 18). In this respect, the position accuracy is interesting to study against the invasiveness to illuminate the link between accuracy requirement and impact on the body (Figure 35). A global affine correlation seems to emerge: the invasiveness decreases when the accuracy increases (except for the microscope and the ultrafast Doppler tomography which use a skull window to work). In fact, the most precise systems use smaller embedded elements directly favouring the noninvasiveness. Moreover, the only non-invasive systems (CT and MRI) which appear on the chart are currently the most widely used all over the world, demonstrating the importance of invasiveness in the current medicine.

To draw the most accurate picture of the field, performance and invasiveness (Figure 34 and 35, respectively) are crossed with physics.
The magnetic field family (Son et al., 2016; Plotkin and Paperno, 2003; Dai et al., 2018; Kim et al., 2010), presents position

[20] According to (Farhat et al., 2015), registration describes the process of identifying a transformation that aligns one data set with another, fusing complementary information sources for planning and intraprocedural guidance. For more details on this subject, see (Fitzpatrick, 2010).

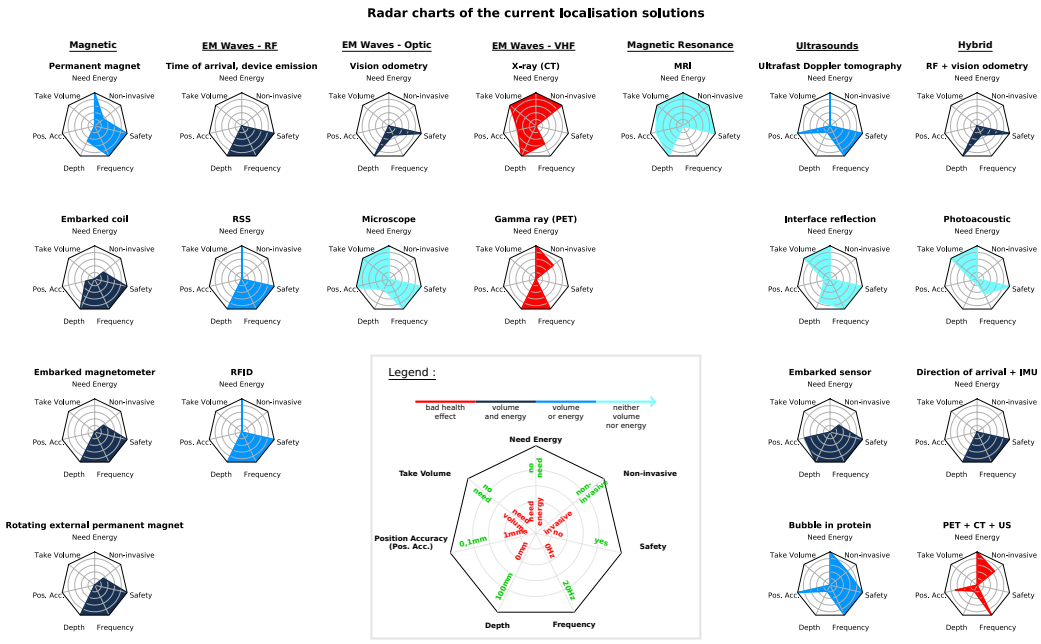

FIGURE 33 Radar charts of the current localisation solutions (corresponding references in Appendix)

accuracy around the millimetre, which is not appropriate for microdevice localisation. The link between the signal strength and the inverse of the cubic travelled distance blocks the technology improvement and caps the achievable accuracy.

The EM RF waves technologies (Pourhomayoun et al., 2014; Wang et al., 2011; Wille et al., 2011) are limited by their centimetric position accuracy, not fitting the microdevice requirements. Position accuracy is directly impacted by the lack of knowledge of the human body refractive index, inserting errors in the position computation. As for the future, until the human body is sufficiently modeled, the EM RF techniques will suffer from such a lack of accuracy.

The EM optical waves family (Bao et al., 2014; Khalil et al., 2014) is subject to strong absorptions in human tissues (Figure 12) limiting the depth of operation and imposing invasiveness to bypass bone layers. The only way to use optical waves in the brain is to embark the system inside the device. Nevertheless, the current technologies are not competitive and need to be improved.

EM VHF waves (Flohr et al., 2004, 2006; Moses, 2011), beyond limit doses, have a bad impact on human tissues, as explained by the WHO (WHO, 2016). This directly prohibits the compatibility with future long-time applications.

MRI technology is capped by its intrinsic trade-off between time and spatial resolutions (Portnoy et al., 2009). Several research teams are focusing on overcoming this trade-off limitation, to develop an ultimate non-invasive imaging technology. The use of MRI prohibits the use of magnetic materials, strongly reducing the number of embeddable systems. To conclude, until a new breakthrough in the field, the MRI use will be limited for micro-medical device tracking.

Ultrasound waves (Demené et al., 2016a,b; Errico et al., 2015; Khalil et al., 2014, 2018; Nikolov and Jensen, 2008; Bourdeau et al., 2018) suffer from attenuation in tissue layers and from reflection at interfaces, limiting the performance trio: invasiveness, position accuracy and depth of use. Recent discoveries enable to break the barrier created by attenuation and reflections, opening a new field of applications called the "neuroimaging" and fitting with micro-medical device

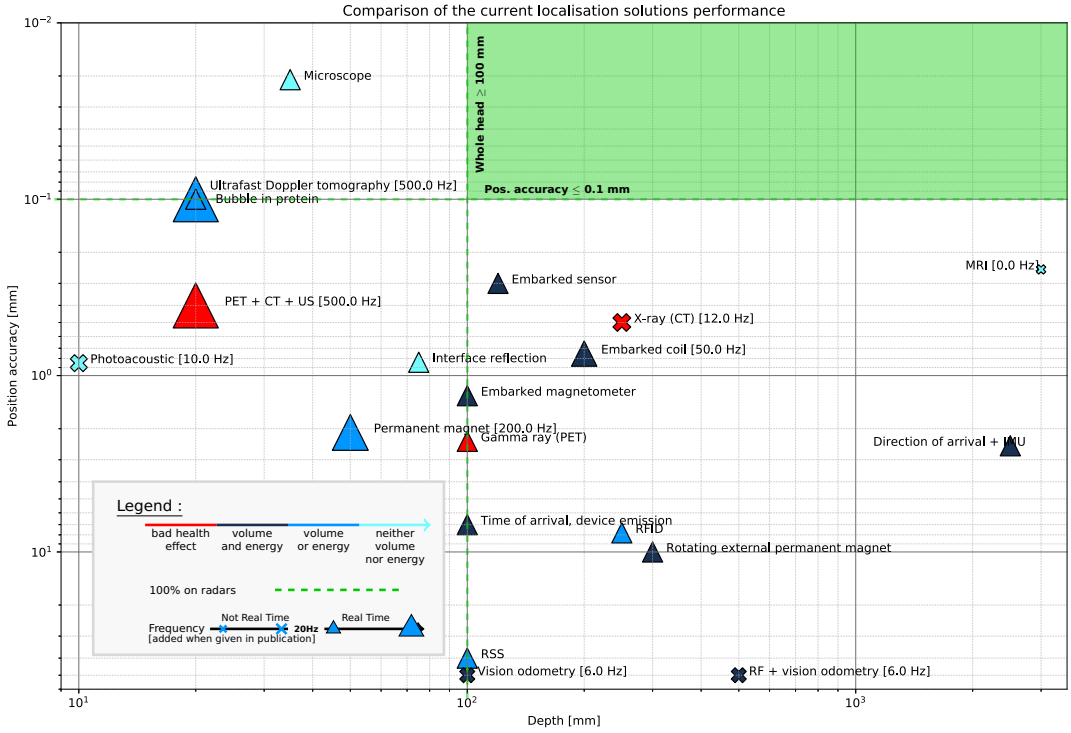

FIGURE 34 Comparison of the current localisation solutions performance (corresponding references in Appendix)

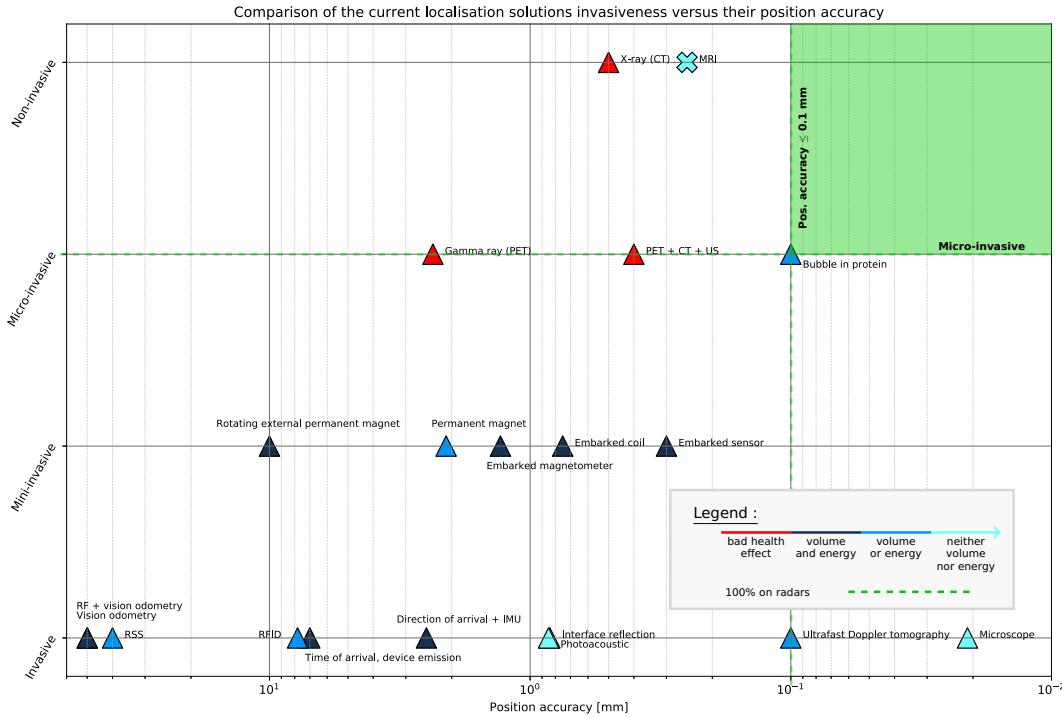

FIGURE 35 Comparison of the current localisation solutions invasiveness versus their position accuracy (corresponding references in Appendix)

requirements. On the other side, ultrasound tracking systems also try to circumvent this barrier through different solutions, which always negatively impact other system's characteristics. In the future, the merging of neuroimaging technologies and tracking systems seems able to overcome the triple dimension trade-off without compromise.
Hybrid systems (Bao et al., 2015; Buehler et al., 2012; Goh et al., 2014; Provost et al., 2018) don't succeed in outperforming the technologies they rely on, and in attenuating their drawbacks. Indeed, each separate technology is not ready to be combined to another one yet and should be intrinsically improved. It is probably for this reason that this field is still emerging.

4 | CONCLUSION

Neurosurgeons cannot reach today deep and functional structures without causing tissue damage. The challenge of deep body operations remains crucial to allow new emerging diagnostic procedures and targeted therapies, such as the identification and treatment of early stage cancers. Besides medicine, big advances on the propulsion and the navigation at the micron scale (Kummer et al., 2010; Khalil et al., 2014; Tottori et al., 2011; Kim et al., 2016; Qiu et al., 2015; Ahmed et al., 2016; Villangca et al., 2016; Dai et al., 2016; Solovev et al., 2009; Magdanz et al., 2015) open the way to neurosurgery operations by micromachines. Deep operations with microdevices, to be suitable for clinical use, need a sub-millimetre tracking system, providing localisation in such heterogeneous and changing environments (Mariana Medina-Sànchez and Oliver G. Schmidt, 2017).

In the present paper, tracking systems for the whole body were listed and each family was described : magnetic field, EM optical waves and MRI families are, today, limited by the physics and the current technologies; EM RF waves family suffers from a lack of models of the human body; EM VHF waves have a bad effect on human body; ultrasound technologies are still emerging; and hybrid systems show the same lack of the systems they combine.
Systems were also compared, as for therapy needs (Figure 32), performance (Figure 34) and invasiveness (Figure 35). A diagonal line caps the current systems performance, demonstrating the present trade-off between accuracy, depth and frequency whereas therapies requirements (Figure 32) highlight the need to overcome this limit. Moreover, the evaluation of the invasiveness (Figure 35) showed that the facility of use is a major issue for clinicians to decide to adopt a specific system and that the higher the accuracy the less invasive the system.

All those reflections introduce a three sides challenge that tracking systems for intracranial medical devices have to deal with: performance (position accuracy, depth, frequency), invasiveness (impact on performance and patient comfort) and user experience (easy applicable to patient and easy reproducible). The future of the neurosurgery will pass by the development of localisation systems fitting these requirements and allowing to widely spread out new localised therapies as deep brain stimulation (Hariz et al., 2013) and gene therapies (Hocquemiller et al., 2016). section conclusion (end)

APPENDIX

Table 4 shows the correspondence between Figure 33, 34, 35 labels and references number.

Labels in Figure 33, 34, 35	**Reference**
Permanent Magnet	(Son et al., 2016)

Embarked coil	(Plotkin and Paperno, 2003)
Embarked magnetometer	(Dai et al., 2018)
Rotating external permanent magnet	(Kim et al., 2010)
Time of arrival, device emission	(Pourhomayoun et al., 2014)
RSS	(Wang et al., 2011)
RFID	(Wille et al., 2011)
Vision odometry	(Bao et al., 2014)
Microscope	(Khalil et al., 2014)
X-ray (CT)	(Flohr et al., 2006)
Gamma ray (PET)	(Moses, 2011)
MRI	(Stucht et al., 2015)
Ultrafast Doppler Tomography	(Demené et al., 2016a)
Interface reflection	(Khalil et al., 2018)
Embarked sensor	(Nikolov and Jensen, 2008)
Bubble in protein	(Bourdeau et al., 2018)
RF + vision odometry	(Bao et al., 2015)
Photoacoustic	(Buehler et al., 2012)
Direction of arrival + IMU	(Goh et al., 2014)
PET + CT + US	(Provost et al., 2018)

TABLE 4 Correspondence between Figure 33, 34, 35 and references

ACKNOWLEDGMENT

The authors would like to thank Mario Aricó, Davide Caimmi, Giulia Turchi and Ali Oulmas for their several revisions and advices about the writing.

BIOGRAPHIES

QUENTIN FRANÇOIS received his Master degree in Mechatronics Engineering from the National Institute of Applied Sciences (INSA), Strasbourg, France in 2017. He is currently a PhD CIFRE student at the Institute of Intelligent Systems and Robotics (ISIR), Sorbonne University and at Robeauté, Paris, France. He also is in charge of the tracking, the guidance and the user interface sides at Robeauté. His current research is focused on microrobotics control and tracking for the medical domain.

ARTHUR ANDRÉ received his Master Degree from the University of Pierre and Marie Curie, Medicine Faculty, Paris, France in 2014. He has been a neurosurgeon fellow in the neurosurgery department of Pr. Carpentier in La Pitié-Salpêtrière hospital, Paris, France since 2015. He also received Master degrees in Integrative Biology and Physiology and in Neurosciences from the University of Pierre

and Marie Curie in 2005 and 2012, respectively. He is currently working towards his second PhD degree at Paris-Saclay University in the Medicine, Health, Biology and Cancerology school.s

BERTRAND DUPLAT received his Master degree in Engineering from the National School of Advanced Techniques (ENSTA), Paris, France in 1990. He worked as a researcher in Robotics, Perception, and 3D interactivity at McGill University, Montréal, Canada from 1991 to 1993. He has been founder, CTO, CEO, President and Vice President of several new technologies companies since 1993 including Virtools, Dassault Systèmes, Dreem, and is currently founder and CEO of Robeauté. His research interests are focused on microrobotics for the medical domain.

SINAN HALIYO obtained his PhD degree in Micromanipulation from the University of Pierre and Marie Curie, Paris, France in 1999. He is an associate professor at Institute of Intelligent Systems and Robotics (ISIR), Sorbonne University and has been active in the field of microrobotics since 1999. His main topics include control and design issues, physical interactions and user interfaces for microscale applications in assembly, characterization and user training. He also takes a particular interest on human-computer interaction issues in remote handling and teleoperation, especially with haptics and multimodal interfaces.

STÉPHANE RÉGNIER received his PhD degree in Mechanics and Robotics from the University of Pierre and Marie Curie, Paris, France in 1996. He is currently Professor at the Institute of Intelligent Systems and Robotics (ISIR), Sorbonne University, Paris, France. He has been head of the ISIR micromanipulation team since 2001. His research interests are focused on micro and nano manipulation, teleoperation and haptic feedback at the nanoscale, micromechatronics and biological cell characterization.

REFERENCES

Ahmed, D., Baasch, T., Jang, B., Pane, S., Dual, J. and Nelson, B. J. (2016) Artificial Swimmers Propelled by Acoustically Activated Flagella. *Nano Letters*, **16**, 4968–4974. URL: https://doi.org/10.1021/acs.nanolett.6b01601.

Bao, G., Mi, L., Geng, Y., Zhou, M. and Pahlavan, K. (2014) A video-based speed estimation technique for localizing the wireless capsule endoscope inside gastrointestinal tract. *Conference proceedings: ... Annual International Conference of the IEEE Engineering in Medicine and Biology Society. IEEE Engineering in Medicine and Biology Society. Annual Conference*, **2014**, 5615–5618.

Bao, G., Pahlavan, K. and Mi, L. (2015) Hybrid Localization of Microrobotic Endoscopic Capsule Inside Small Intestine by Data Fusion of Vision and RF Sensors. *IEEE Sensors Journal*, **15**, 2669–2678.

Bourdeau, R. W., Lee-Gosselin, A., Lakshmanan, A., Farhadi, A., Kumar, S. R., Nety, S. P. and Shapiro, M. G. (2018) Acoustic reporter genes for noninvasive imaging of microorganisms in mammalian hosts. *Nature*, **553**, 86. URL: https://www.nature.com/articles/nature25021.

Buehler, A., Deán-Ben, X. L., Claussen, J., Ntziachristos, V. and Razansky, D. (2012) Three-dimensional optoacoustic tomography at video rate. *Optics Express*, **20**, 22712–22719. URL: https://www.osapublishing.org/abstract.cfm?uri=oe-20-20-22712.

Bushby, K. M., Cole, T., Matthews, J. N. and Goodship, J. A. (1992) Centiles for adult head circumference. *Archives of Disease in Childhood*, **67**, 1286–1287. URL: https://www.ncbi.nlm.nih.gov/pmc/articles/PMC1793909/.

Chaillet, N. and Stéphane, R. (2013) *Microrobotics for Micromanipulation*. Wiley-Blackwell.

Chen, X.-Z., Jang, B., Ahmed, D., Hu, C., Marco, C. D., Hoop, M., Mushtaq, F., Nelson, B. J. and Pané, S. (2018) Small-Scale Machines Driven by External Power Sources. *Advanced Materials*, **30**, 1705061. URL: https://onlinelibrary.wiley.com/doi/abs/10.1002/adma.201705061.

Dai, B., Wang, J., Xiong, Z., Zhan, X., Dai, W., Li, C.-C., Feng, S.-P. and Tang, J. (2016) Programmable artificial phototactic microswimmer. *Nature Nanotechnology*, **11**, 1087–1092. URL: https://www.nature.com/articles/nnano.2016.187.

Dai, H., Song, S., Zeng, X., Su, S., Lin, M. and Meng, M. Q. H. (2018) 6-D Electromagnetic Tracking Approach Using Uniaxial Transmitting Coil and Tri-Axial Magneto-Resistive Sensor. *IEEE Sensors Journal*, **18**, 1178–1186.

Deffieux, T., Demene, C., Pernot, M. and Tanter, M. (2018) Functional ultrasound neuroimaging: a review of the preclinical and clinical state of the art. *Current Opinion in Neurobiology*, **50**, 128–135. URL: https://www.sciencedirect.com/science/article/pii/S0959438817302465.

Demené, C., Bimbard, C., Gesnik, M., Radtke-Schuller, S., Shamma, S., Boubenec, Y. and Tanter, M. (2016a) Functional Ultrasound Imaging of the thalamo-cortical auditory tract in awake ferrets using ultrafast Doppler imaging. In *2016 IEEE International Ultrasonics Symposium (IUS)*, 1–4.

Demené, C., Tiran, E., Sieu, L.-A., Bergel, A., Gennisson, J. L., Pernot, M., Deffieux, T., Cohen, I. and Tanter, M. (2016b) 4d microvascular imaging based on ultrafast Doppler tomography. *NeuroImage*, **127**, 472–483.

Ding, H., Lu, J. Q., Wooden, W. A., Kragel, P. J. and Hu, X.-H. (2006) Refractive indices of human skin tissues at eight wavelengths and estimated dispersion relations between 300 and 1600 nm. *Physics in Medicine and Biology*, **51**, 1479–1489.

Ehrenberg, M. (2014) SUPER-RESOLVED FLUORESCENCE MICROSCOPY. *Scientific Background on the Nobel Prize in Chemistry 2014*, The Royal Swedish Academy of Sciences. URL: https://www.nobelprize.org/uploads/2018/06/advanced-chemistryprize2014.pdf.

Errico, C., Pierre, J., Pezet, S., Desailly, Y., Lenkei, Z., Couture, O. and Tanter, M. (2015) Ultrafast ultrasound localization microscopy for deep super-resolution vascular imaging. *Nature*, **527**, 499. URL: https://www.nature.com/articles/nature16066.

Farhat, N., Kapur, T. and Kikinis, R. (2015) Chapter 6 - Role of Computers and Image Processing in Image-Guided Brain Tumor Surgery. In *Image-Guided Neurosurgery* (ed. A. J. Golby), 143–161. Boston: Academic Press. URL: http://www.sciencedirect.com/science/article/pii/B9780128008706000066.

Feynman, R. (1963) *The Feynman Lectures on Physics: Volume 2*, vol. 2 of *The Feynman Lectures on Physics*. Boston: Addison-Wesley.

Fitzpatrick, J. M. (2010) The role of registration in accurate surgical guidance. *Proceedings of the Institution of Mechanical Engineers. Part H, Journal of Engineering in Medicine*, **224**, 607–622.

Flohr, T., Stierstorfer, K., Raupach, R., Ulzheimer, S. and Bruder, H. (2004) Performance Evaluation of a 64-Slice CT System with z-Flying Focal Spot. *RöFo - Fortschritte auf dem Gebiet der Röntgenstrahlen und der bildgebenden Verfahren*, **176**, 1803–1810. URL: http://www.thieme-connect.de/DOI/DOI?10.1055/s-2004-813717.

Flohr, T. G., McCollough, C. H., Bruder, H., Petersilka, M., Gruber, K., Süβ, C., Grasruck, M., Stierstorfer, K., Krauss, B., Raupach, R., Primak, A. N., Küttner, A., Achenbach, S., Becker, C., Kopp, A. and Ohnesorge, B. M. (2006) First performance evaluation of a dual-source CT (DSCT) system. *European Radiology*, **16**, 256–268. URL: http://link.springer.com/10.1007/s00330-005-2919-2.

Goh, S. T., Zekavat, S. A. . and Pahlavan, K. (2014) DOA-Based Endoscopy Capsule Localization and Orientation Estimation via Unscented Kalman Filter. *IEEE Sensors Journal*, **14**, 3819–3829.

Goldman, L. W. (2007) Principles of CT and CT Technology. *Journal of Nuclear Medicine Technology*, **35**, 115–128. URL: http://tech.snmjournals.org/cgi/doi/10.2967/jnmt.107.042978.

Gumprecht, J. D. J., Lueth, T. C. and Khamesee, M. B. (2013) Navigation of a robotic capsule endoscope with a novel ultrasound tracking system. *Microsystem Technologies*, **19**, 1415–1423. URL: https://link.springer.com/article/10.1007/s00542-013-1828-6.

Hariz, M., Blomstedt, P. and Zrinzo, L. (2013) Future of brain stimulation: New targets, new indications, new technology. *Movement Disorders*, **28**, 1784–1792. URL: https://onlinelibrary.wiley.com/doi/abs/10.1002/mds.25665.

Hasgall, P., Di Gennaro, F., Baumgartner, C., Neufeld, E., Lloyd, B., Gosselin, M., Payne, D., Klingenböck, A. and Kuster, N. (2018) Tissue Properties Database V4.0. *IT'IS Foundation*. URL: https://itis.swiss/virtual-population/tissue-properties/. Version 4.0.

Himes, N. C. and Young, G. (2015) Chapter 2 - Background on Imaging Structural Imaging. In *Image-Guided Neurosurgery* (ed. A. J. Golby), 25–61. Boston: Academic Press. URL: http://www.sciencedirect.com/science/article/pii/B9780128008706000029.

Hocquemiller, M., Giersch, L., Audrain, M., Parker, S. and Cartier, N. (2016) Adeno-Associated Virus-Based Gene Therapy for CNS Diseases. *Human Gene Therapy*, **27**, 478–496. URL: https://www.liebertpub.com/doi/abs/10.1089/hum.2016.087.

Huang, B., Law, M. W.-M. and Khong, P.-L. (2009) Whole-Body PET/CT Scanning: Estimation of Radiation Dose and Cancer Risk. *Radiology*, **251**, 166–174. URL: https://pubs.rsna.org/doi/10.1148/radiol.2511081300.

Huber, D., Petreanu, L., Ghitani, N., Ranade, S., Hromádka, T., Mainen, Z. and Svoboda, K. (2008) Sparse optical microstimulation in barrel cortex drives learned behaviour in freely moving mice. *Nature*, **451**, 61–64.

Hämäläinen, M., Hari, R., Ilmoniemi, R. J., Knuutila, J. and Lounasmaa, O. V. (1993) Magnetoencephalography—theory, instrumentation, and applications to noninvasive studies of the working human brain. *Reviews of Modern Physics*, **65**, 413–497. URL: https://link.aps.org/doi/10.1103/RevModPhys.65.413.

Kawasaki, M. and Kohno, R. (2009) A TOA Based Positioning Technique of Medical Implanted Devices. In *in Third international Symposium on Medical information & communication technology*.

Khalil, I. S. M., Ferreira, P., Eleutério, R., Korte, C. L. d. and Misra, S. (2014) Magnetic-based closed-loop control of paramagnetic microparticles using ultrasound feedback. In *2014 IEEE International Conference on Robotics and Automation (ICRA)*, 3807–3812.

Khalil, I. S. M., Mahdy, D., Sharkawy, A. E., Moustafa, R. R., Tabak, A. F., Mitwally, M. E., Hesham, S., Hamdi, N., Klingner, A., Mohamed, A. and Sitti, M. (2018) Mechanical Rubbing of Blood Clots Using Helical Robots Under Ultrasound Guidance. *IEEE Robotics and Automation Letters*, **3**, 1112–1119.

Kim, M.-G., Hong, Y.-S. and Lim, E.-J. (2010) Position and orientation detection of capsule endoscopes in spiral motion. *International Journal of Precision Engineering and Manufacturing*, **11**, 31–37. URL: https://link.springer.com/article/10.1007/s12541-010-0004-5.

Kim, S., Lee, S., Lee, J., Nelson, B. J., Zhang, L. and Choi, H. (2016) Fabrication and Manipulation of Ciliary Microrobots with Non-reciprocal Magnetic Actuation. *Scientific Reports*, **6**, 30713. URL: https://www.nature.com/articles/srep30713.

Kneipp, M., Turner, J., Estrada, H., Rebling, J., Shoham, S. and Razansky, D. (2016) Effects of the murine skull in optoacoustic brain microscopy. *Journal of Biophotonics*, **9**, 117–123.

Kummer, M. P., Abbott, J. J., Kratochvil, B. E., Borer, R., Sengul, A. and Nelson, B. J. (2010) OctoMag: An Electromagnetic System for 5-DOF Wireless Micromanipulation. *IEEE Transactions on Robotics*, **26**, 1006–1017.

Li, Y. (2012) *Tag Position Estimation in RFID Systems*. Master's thesis, The University of Adelaide, Australia.

Liang Mi, Guanqun Bao and Kaveh Pahlavan (2014) Geometric estimation of intestinal contraction for motion tracking of video capsule endoscope. vol. 9036, 90360B–9036–10. SPIE. URL: https://doi.org/10.1117/12.2043963.

Lillie, E. M., Urban, J. E., Weaver, A. A., Powers, A. K. and Stitzel, J. D. (2015) Estimation of skull table thickness with clinical CT and validation with microCT. *Journal of Anatomy*, **226**, 73–80. URL: https://www.ncbi.nlm.nih.gov/pmc/articles/PMC4313900/.

Lu, Y., Yeung, C., Radmanesh, A., Wiemann, R., Black, P. M. and Golby, A. J. (2015) Comparative effectiveness of frame-based, frameless, and intraoperative magnetic resonance imaging-guided brain biopsy techniques. *World Neurosurgery*, **83**, 261–268.

Magdanz, V., Medina-Sánchez, M., Chen, Y., Guix, M. and Schmidt, O. G. (2015) How to Improve Spermbot Performance. *Advanced Functional Materials*, **25**, 2763–2770. URL: https://onlinelibrary.wiley.com/doi/abs/10.1002/adfm.201500015.

Manohara, S. R., Hanagodimath, S. M. and Gerward, L. (2011) Energy absorption buildup factors of human organs and tissues at energies and penetration depths relevant for radiotherapy and diagnostics. *Journal of Applied Clinical Medical Physics*, **12**, 296–312. URL: http://doi.wiley.com/10.1120/jacmp.v12i4.3557.

Mariana Medina-Sànchez and Oliver G. Schmidt (2017) Medical microbots need better imaging and control. *Nature*, **545**, 406 – 408. URL: https://www.nature.com/news/medical-microbots-need-better-imaging-and-control-1.22022.

Michel, E., Hernandez, D. and Lee, S. Y. (2017) Electrical conductivity and permittivity maps of brain tissues derived from water content based on T1-weighted acquisition. *Magnetic Resonance in Medicine*, **77**, 1094–1103. URL: http://onlinelibrary.wiley.com/doi/10.1002/mrm.26193/abstract.

Morel, J.-M. and Yu, G. (2009) ASIFT: A New Framework for Fully Affine Invariant Image Comparison. *SIAM Journal on Imaging Sciences*, **2**, 438–469. URL: http://epubs.siam.org/doi/10.1137/080732730.

Moses, W. W. (2011) Fundamental Limits of Spatial Resolution in PET. *Nuclear instruments & methods in physics research. Section A, Accelerators, spectrometers, detectors and associated equipment*, **648 Supplement 1**, S236–S240. URL: https://www.ncbi.nlm.nih.gov/pmc/articles/PMC3144741/.

Nikolov, S. I. and Jensen, J. A. (2008) Precision of needle tip localization using a receiver in the needle. In *2008 IEEE Ultrasonics Symposium*, 479–482.

Oulmas, A., Andreff, N. and Régnier, S. (2018) 3d closed-loop swimming at low Reynolds numbers. *The International Journal of Robotics Research*, **37**, 0278364918801502. URL: https://doi.org/10.1177/0278364918801502.

Plotkin, A. and Paperno, E. (2003) 3-D magnetic tracking of a single subminiature coil with a large 2-D array of uniaxial transmitters. *IEEE Transactions on Magnetics*, **39**, 3295–3297.

Portnoy, S., Kale, S. C., Feintuch, A., Tardif, C., Pike, G. B. and Henkelman, R. M. (2009) Information content of SNR/resolution trade-offs in three-dimensional magnetic resonance imaging: Information content of SNR/resolution trade-offs in 3d MRI. *Medical Physics*, **36**, 1442–1451. URL: http://doi.wiley.com/10.1118/1.3098124.

Pourhomayoun, M., Jin, Z. and Fowler, M. L. (2014) Accurate localization of in-body medical implants based on spatial sparsity. *IEEE transactions on bio-medical engineering*, **61**, 590–597.

Provost, J., Garofalakis, A., Sourdon, J., Bouda, D., Berthon, B., Viel, T., Perez-Liva, M., Lussey-Lepoutre, C., Favier, J., Correia, M., Pernot, M., Chiche, J., Pouysségur, J., Tanter, M. and Tavitian, B. (2018) Simultaneous positron emission tomography and ultrafast ultrasound for hybrid molecular, anatomical and functional imaging. *Nature Biomedical Engineering*, **2**, 85–94. URL: https://www.nature.com/articles/s41551-018-0188-z.

Qiu, F., Fujita, S., Mhanna, R., Zhang, L., Simona, B. R. and Nelson, B. J. (2015) Magnetic Helical Microswimmers Functionalized with Lipoplexes for Targeted Gene Delivery. *Advanced Functional Materials*, **25**, 1666–1671. URL: https://onlinelibrary.wiley.com/doi/abs/10.1002/adfm.201403891.

Rich, S. I., Wood, R. J. and Majidi, C. (2018) Untethered soft robotics. *Nature Electronics*, **1**, 102–112. URL: https://www.nature.com/articles/s41928-018-0024-1.

Rohen, J. W., Yokochi, C. and Lütjen-Drecoll, E. (1998) *Color Atlas of Anatomy: A Photographic Study of the Human Body*. 7. Schattauer, wolters kluwer health edn.

Röschmann, P. (1987) Radiofrequency penetration and absorption in the human body: Limitations to high-field whole-body nuclear magnetic resonance imaging. *Medical Physics*, **14**, 922–931. URL: https://aapm.onlinelibrary.wiley.com/doi/abs/10.1118/1.595995.

Saleh, B. E. A. and Teich, M. C. (2001) Electromagnetic Optics. In *Fundamentals of Photonics*, 157–195. Wiley-Blackwell, j.w.goodman edn. URL: https://onlinelibrary.wiley.com/doi/abs/10.1002/0471213748.ch5.

Sanai, N. and Berger, M. S. (2008) Glioma extent of resection and its impact on patient outcome. *Neurosurgery*, **62**, 753–766. URL: https://academic.oup.com/neurosurgery/article/62/4/753/2564146.

Sayrafian-Pour, K., Yang, W. B., Hagedorn, J., Terrill, J. and Yazdandoost, K. Y. (2009) A statistical path loss model for medical implant communication channels. In *2009 IEEE 20th International Symposium on Personal, Indoor and Mobile Radio Communications*, 2995–2999.

Shevzov-Zebrun, N., Brennan, N. M. P., Peck, K. K. and Holodny, A. I. (2015) Chapter 3 - Advanced Functional Imaging: fMRI, PET, and MEG. In *Image-Guided Neurosurgery* (ed. A. J. Golby), 63–89. Boston: Academic Press. URL: http://www.sciencedirect.com/science/article/pii/B9780128008706000030.

Solovev, A. A., Mei, Y., Bermúdez Ureña, E., Huang, G. and Schmidt, O. G. (2009) Catalytic microtubular jet engines self-propelled by accumulated gas bubbles. *Small (Weinheim an Der Bergstrasse, Germany)*, **5**, 1688–1692.

Son, D., Yim, S. and Sitti, M. (2016) A 5-D Localization Method for a Magnetically Manipulated Untethered Robot Using a 2-D Array of Hall-Effect Sensors. *IEEE/ASME Transactions on Mechatronics*, **21**, 708–716.

Stucht, D., Danishad, K. A., Schulze, P., Godenschweger, F., Zaitsev, M. and Speck, O. (2015) Highest Resolution In Vivo Human Brain MRI Using Prospective Motion Correction. *PLoS ONE*, **10**. URL: https://www.ncbi.nlm.nih.gov/pmc/articles/PMC4520483/.

Taylor, R. H., Menciassi, A., Fichtinger, G., Fiorini, P. and Dario, P. (2016) Medical Robotics and Computer-Integrated Surgery. In *Springer Handbook of Robotics*, 1657–1684. Springer, Cham.

Than, T. D., Alici, G., Zhou, H. and Li, W. (2012) A Review of Localization Systems for Robotic Endoscopic Capsules. *IEEE Transactions on Biomedical Engineering*, **59**, 2387–2399.

Tottori, S., Sugita, N., Kometani, R., Ishihara, S. and Mitsuishi, M. (2011) Selective control method for multiple magnetic helical microrobots. *Journal of Micro-Nano Mechatronics*, **6**, 89–95. URL: https://doi.org/10.1007/s12213-011-0035-8.

Valentin, J. and on Radiological Protection, I. C. (eds.) (2007) *The 2007 recommendations of the International Commission on Radiological Protection*. No. 103 in ICRP publication. Oxford: Elsevier. OCLC: 220472854.

Villangca, M. J., Palima, D., Bañas, A. R. and Glückstad, J. (2016) Light-driven micro-tool equipped with a syringe function. *Light: Science & Applications*, **5**, e16148. URL: https://www.nature.com/articles/lsa2016148.

Wakana, S., Jiang, H., Nagae-Poetscher, L. M., van Zijl, P. C. M. and Mori, S. (2004) Fiber Tract–based Atlas of Human White Matter Anatomy. *Radiology*, **230**, 77–87. URL: http://pubs.rsna.org/doi/10.1148/radiol.2301021640.

Wang, Y., Fu, R., Ye, Y., Khan, U. and Pahlavan, K. (2011) Performance bounds for RF positioning of endoscopy camera capsules. In *2011 IEEE Topical Conference on Biomedical Wireless Technologies, Networks, and Sensing Systems*, 71–74.

WHO (2016) Ionizing radiation, health effects and protective measures. URL: http://www.who.int/en/news-room/fact-sheets/detail/ionizing-radiation-health-effects-and-protective-measures.

Wille, A., Broll, M. and Winter, S. (2011) Phase difference based RFID navigation for medical applications. In *2011 IEEE International Conference on RFID*, 98–105.

Xia, J., Yao, J. and Wang, L. V. (2014) Photoacoustic tomography: principles and advances. *Electromagnetic waves (Cambridge, Mass.)*, **147**, 1–22. URL: https://www.ncbi.nlm.nih.gov/pmc/articles/PMC4311576/.

Yizhar, O., Fenno, L., Davidson, T., Mogri, M. and Deisseroth, K. (2011) Optogenetics in Neural Systems. *Neuron*, **71**, 9–34. URL: http://linkinghub.elsevier.com/retrieve/pii/S0896627311005046.

Young, A. R. (1997) Chromophores in human skin. *Physics in Medicine and Biology*, **42**, 789–802.

Zeineh, M., Parekh, M., Zaharchuk, G., Su, J., Rosenberg, J., Fischbein, N. and Rutt, B. (2014) Ultra-High Resolution Imaging of the Human Brain with Phase-Cycled Balanced Steady State Free Precession at 7.0t. *Investigative radiology*, **49**, 278–289. URL: https://www.ncbi.nlm.nih.gov/pmc/articles/PMC4311399/.

Ziskin, M. C. (1993) Fundamental physics of ultrasound and its propagation in tissue. *Radiographics: A Review Publication of the Radiological Society of North America, Inc*, **13**, 705–709.